GEOLOGY

Globally distributed iridium layer preserved within the Chicxulub impact structure

Steven Goderis[1]*, Honami Sato[2,3], Ludovic Ferrière[4], Birger Schmitz[5], David Burney[6], Pim Kaskes[1,7], Johan Vellekoop[1,8], Axel Wittmann[9], Toni Schulz[10,11], Stepan M. Chernonozhkin[12], Philippe Claeys[1], Sietze J. de Graaff[1,7], Thomas Déhais[1,7], Niels J. de Winter[1,13], Mikael Elfman[5], Jean-Guillaume Feignon[10], Akira Ishikawa[14,3], Christian Koeberl[10], Per Kristiansson[5], Clive R. Neal[6], Jeremy D. Owens[15], Martin Schmieder[16,17], Matthias Sinnesael[1,18], Frank Vanhaecke[12], Stijn J. M. Van Malderen[12], Timothy J. Bralower[19], Sean P. S. Gulick[20,21,22], David A. Kring[17], Christopher M. Lowery[20], Joanna V. Morgan[23], Jan Smit[24], Michael T. Whalen[25], IODP-ICDP Expedition 364 Scientists†

The Cretaceous-Paleogene (K-Pg) mass extinction is marked globally by elevated concentrations of iridium, emplaced by a hypervelocity impact event 66 million years ago. Here, we report new data from four independent laboratories that reveal a positive iridium anomaly within the peak-ring sequence of the Chicxulub impact structure, in drill core recovered by IODP-ICDP Expedition 364. The highest concentration of ultrafine meteoritic matter occurs in the post-impact sediments that cover the crater peak ring, just below the lowermost Danian pelagic limestone. Within years to decades after the impact event, this part of the Chicxulub impact basin returned to a relatively low-energy depositional environment, recording in unprecedented detail the recovery of life during the succeeding millennia. The iridium layer provides a key temporal horizon precisely linking Chicxulub to K-Pg boundary sections worldwide.

INTRODUCTION

The mass extinction at the Cretaceous-Paleogene (K-Pg) boundary ~66.05 million years ago abruptly and irreversibly reshaped Earth's biosphere (*1*–*4*). In the geologic record, the K-Pg event is marked by a thin layer of clay, found so far in more than 350 marine and terrestrial sections across the globe (Fig. 1) (*3*, *5*, *6*). The boundary clay contains concentrations of iridium (Ir) and the other moderately (e.g., Co and Ni) and highly siderophile elements (HSEs; Ru, Rh, Pd, Re, Os, Pt, and Au) that are anomalously enriched by up to four orders of magnitude relative to continental crustal background levels (*3*, *6*–*8*). The positive Ir anomaly, first measured in the boundary layers of Gubbio (Italy) and Caravaca (Spain), was initially used to propose a large-scale impact of an extraterrestrial body as the cause for the mass extinction (Fig. 1) (*1*, *2*). This Ir layer is now formally the "golden spike" that defines the end of the Cretaceous Period and Mesozoic Era according to the Geological Time Scale (*9*). While HSEs are abundant in primitive asteroids not affected by planetary differentiation, siderophile elements largely partition into the planetary interior during core formation, leaving Earth's mantle and crust variably depleted in these metals [(*7*) and references therein]. The Ir anomaly thus reflects the global dispersal of meteoritic matter following the hypervelocity impact of an asteroid approximately 12 km in diameter (*10*). Various other types of impact ejecta have been recovered from K-Pg event deposits, including impact spherules, some of which contain Ni-rich spinel crystals, and shocked mineral grains (*5*, *6*, *11*). While an assortment of HSE carrier phases has been identified within the boundary clay (including magnesioferrite crystals or other spinel group minerals, microkrystite impact spherules, organic matter, or iron-rich nanophases), Ir and the other siderophile elements were likely transported from the impact site across the globe within airborne microscopic dust and impact vapor condensates (*1*, *11*, *12*). The extraterrestrial matter found in the boundary layer was determined to be of carbonaceous chondritic composition (*7*, *13*, *14*).

In the decade following the discovery of the Ir anomaly, high-energy deposits were identified around the Gulf of Mexico (*15*, *16*) and the Caribbean (*17*), culminating in the discovery of the 180- to 200-km-wide Chicxulub impact structure on the Yucatán Peninsula of Mexico (Fig. 1) (*18*, *19*). The size of the Chicxulub structure and the unique stratigraphy of more than 3 km of carbonate- and sulfate-rich sedimentary rocks on top of granitoid basement led to the release of critical volumes of climatically active gases, dust, and soot from the impact site. These aerosols, along with soot from

[1]Analytical, Environmental, and Geochemistry, Vrije Universiteit Brussel, Brussels, Belgium. [2]Department of Geosciences, University of Padova, Padova, Italy. [3]Submarine Resources Research Center, Research Institute for Marine Resources Utilization, Japan Agency for Marine-Earth Science and Technology, Kanagawa, Japan. [4]Natural History Museum, Vienna, Austria. [5]Astrogeobiology Laboratory, Division of Nuclear Physics, Department of Physics, Lund University, Lund, Sweden. [6]Department of Civil and Environmental Engineering and Earth Sciences, University of Notre Dame, Notre Dame, IN, USA. [7]Laboratoire G-Time, Université Libre de Bruxelles, Brussels, Belgium. [8]Department of Geology, KU Leuven, Leuven, Belgium. [9]Eyring Materials Center, Arizona State University, Tempe, AZ, USA. [10]Department of Lithospheric Research, University of Vienna, Vienna, Austria. [11]Institut für Geologie und Mineralogie, Universität zu Köln, Köln, Germany. [12]Atomic and Mass Spectrometry–A&MS research group, Department of Chemistry, Ghent University, Ghent, Belgium. [13]Department of Earth Sciences, Utrecht University, Utrecht, Netherlands. [14]Department of Earth and Planetary Sciences, Tokyo Institute of Technology, Tokyo, Japan. [15]Department of Earth, Ocean and Atmospheric Science and National High Magnetic Field Laboratory, Florida State University, Tallahassee, FL, USA. [16]HNU Neu-Ulm University of Applied Sciences, Neu-Ulm, Germany. [17]Lunar and Planetary Institute–USRA, Houston, TX, USA. [18]Department of Earth Sciences, Durham University, Durham, UK. [19]Department of Geosciences, Pennsylvania State University, University Park, PA, USA. [20]Institute for Geophysics, University of Texas at Austin, Austin, TX, USA. [21]Department of Geological Sciences, University of Texas at Austin, Austin, TX, USA. [22]Center for Planetary Systems Habitability, University of Texas, Austin, TX, USA. [23]Department of Earth Science and Engineering, Imperial College London, London, UK. [24]Department of Earth Sciences, Vrije Universiteit Amsterdam, Amsterdam, Netherlands. [25]Department of Geosciences, University of Alaska Fairbanks, Fairbanks, AK, USA.
*Corresponding author. Email: steven.goderis@vub.be
†Full list of the Expedition 364 Scientists can be found in the Supplementary Materials.

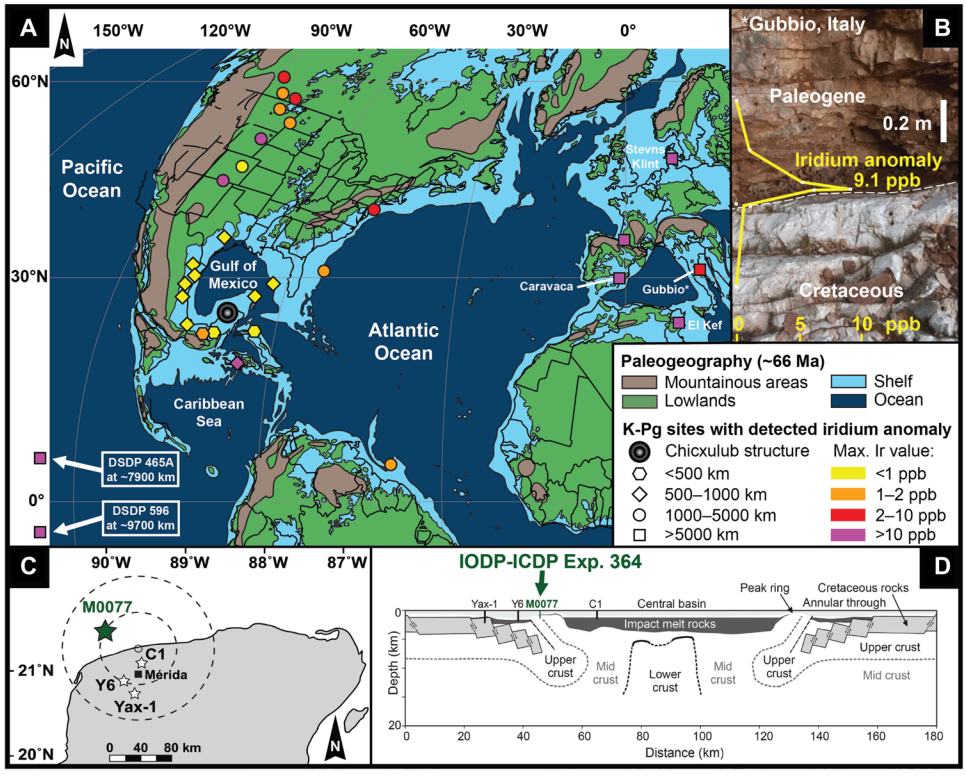

Fig. 1. Location map. (**A**) Paleogeographic reconstruction for the Late Cretaceous with K-Pg ejecta sites distal (>5000 km) to very proximal (<500 km) to the Chicxulub impact structure, displaying sites with a detected Ir anomaly [values based on (*3*, *7*)]. This map is redrawn after (*55*) and updated according to (*56*). All distances as paleogeographic distances between the K-Pg boundary sites and the Chicxulub impact structure. (**B**) Iridium anomaly as measured by (*1*) at the distal Gubbio K-Pg boundary site, Italy. (**C**) Stars designate positions of drill cores on the Yucatán peninsula mentioned in the text (Y6, Yucatán 6; C1, Chicxulub 1; Yax-1, Yaxcopoil-1), including International Ocean Discovery Program (IODP)–International Continental Scientific Drilling Program (ICDP) Expedition 364 (green star). (**D**) Schematic cross section of the Chicxulub crater, with the location of Site M0077 based on (*57*). Photo credit for the image in (B): Heiko Pälike, MARUM-Center for Marine Environmental Sciences, University of Bremen.

wildfires, induced a protracted impact winter governed by reduced solar insolation, global cooling, and acid rain, which greatly reduced photosynthesis in plants and phytoplankton leading to food chain collapse and ocean acidification (*20*, *21*). The stratigraphy of the K-Pg boundary event deposits and distribution of ejecta vary with distance and direction from the Chicxulub crater, with considerable differences between proximal and distal sites, less than 1000 and more than 5000 km from the impact site, respectively (Fig. 1) (*3*, *5*, *6*). In the distal and mostly marine sections, the K-Pg boundary is composed of a ~3-mm-thick reddish clay layer containing shocked minerals, impact spherules, and a distinct Ir concentration peak marking the boundary (*3*, *5*). In more proximal sites, including those around the Gulf of Mexico, the K-Pg boundary typically consists of a series of centimeter- to tens of meter-thick clastic event beds indicative of high-energy sediment transport, such as tsunami and gravity flows, with broader and more moderate Ir anomalies diluted by materials delivered by lower-energy processes, such asseiche waves (fig. S1) (*3*, *6*, *15*–*17*). To date, unambiguous Ir enrichments similar in magnitude to those identified at proximal to distal K-Pg sites have not been reported from within the Chicxulub structure.

In 2016, the International Ocean Discovery Program (IODP) and the International Continental Scientific Drilling Program (ICDP) jointly drilled into the peak ring of the Chicxulub impact structure, offshore of the Yucatán Peninsula at Site M0077 (21.45°N, 89.95°W), and successfully recovered a continuous core from 505.7 to 1334.7 meters below seafloor (mbsf) (Fig. 2) (*22*, *23*). Here, we mainly focus on the siderophile and chalcophile element distribution in Core 40R, Section 1, recovered between 616.24 and 617.68 mbsf. This unique core interval contains the transition from seiche and tsunami deposits to post-impact pelagic limestone in a ~75-cm-thick "transitional unit" (*24*, *25*), sandwiched between resurged impactites below and pelagic marine sediments above (*22*, *23*). We report here the detection of a pronounced positive Ir anomaly that is clearly identified near the top of the transitional unit, together with enrichments in other siderophile and chalcophile elements, which are associated with intervals containing Ni-rich sulfides (Fig. 3). This result conclusively ties Chicxulub to the global Ir layer and K-Pg boundary sections worldwide, thereby confirming the link between crater formation and the Ir peak detected in these sections that record the K-Pg mass extinction. The delivery of Ir by microscopic dust that circled Earth (*12*) before returning to the impact site places important time constraints of less than a few decades on the deposition of the transitional unit and underlying lithological units sampled in the drill core. Core 40R-1 contains an extremely well-preserved record of the immediate aftermath of the Chicxulub impact event within the crater that can be disentangled using various geochemical tracers, including high-resolution HSE concentrations and osmium isotope ratios ($^{187}Os/^{188}Os$). By applying these tracers, the effects of asteroid impacts on the biosphere and global environment in the first months to millennia of the Cenozoic Era as well as

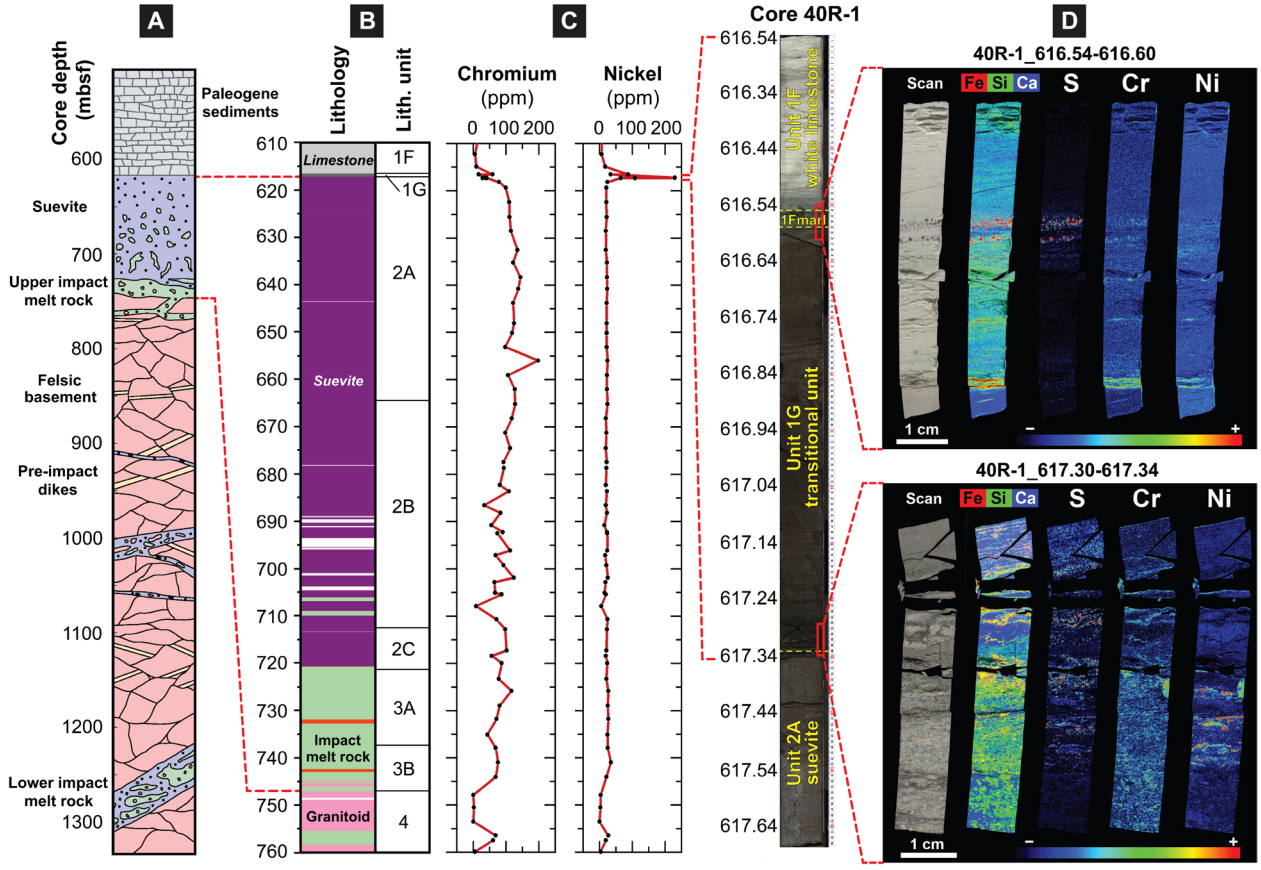

Fig. 2. IODP-ICDP Expedition 364 core overview and geochemical profiles. (**A**) Lithology recovered from drill core at Site M0077 from 505 mbsf to total depth, with Paleogene sediments (gray), suevite (purple), impact melt rock (green), felsic (granitic) basement (pink), and pre-impact dikes (yellow), adapted after (*22*). (**B**) Subdivision of the upper peak-ring interval into various lithological units following (*23*). (**C**) Concentration profiles for chromium and nickel, data from (*23*). Nickel concentration peak detailed in Fig. 3. (**D**) Inset highlighting Core 40R-1, with core intervals displaying siderophile element enrichments, as indicated by μXRF mapping. The high-resolution line scan photo is from the onshore science party (*23*).

the fate of the Chicxulub impactor are unraveled in unprecedented detail.

RESULTS

Core stratigraphy

Site M0077 (21.45°N, 89.95°W) is located offshore of the Yucatán Peninsula above the Chicxulub peak ring (Fig. 1) (*22*, *23*). Chicxulub is characterized by a uniquely preserved peak ring, 80 to 90 km in diameter, and the drill site was selected to address a number of scientific objectives, including testing models of peak ring formation (*22*, *26*). The drill core includes approximately 110 m of post-impact Paleogene hemipelagic and pelagic sedimentary rocks of early Eocene (Ypresian) to earliest Paleocene (Danian) age, 130 m of suevite and impact melt rock (upper peak-ring interval), and 610 m of shocked granitic basement rocks, intruded by magmatic pre-impact dikes and intercalated with impact melt rocks (*22*, *23*, *27*). Unlike the 2002 ICDP Yaxcopoil-1 core, drilled onshore approximately 60 km south-southwest of the center in the annular moat between the peak ring and the outer crater rim, Site M0077 is located within a depression on top of the peak ring (Fig. 1). Unexpectedly, this site recorded minimal evidence of mass wasting from the crater rim or peak ring summits, leading to the recovery of a relatively complete K-Pg boundary sequence within the Chicxulub structure that is preserved at a relatively shallow burial depth (*22*–*25*, *27*–*29*). The uppermost ~3.5 m (620.88 to 617.33 mbsf, Core 40R-1 to 41R-1) of the impact deposits present at Site M0077 is mostly composed of fine-grained, well-sorted, reworked, and bedded suevite (uppermost part of Unit 2A) rich in altered (once vitric) impact melt clasts and isolated Cretaceous foraminifera (fig. S1) (*23*, *24*, *27*, *29*). Above Unit 2A, the ~75-cm transitional unit, composed of generally fining-upward, laminated dark brown to dark grayish brown carbonate-rich silty claystone to micrite (Unit 1G; 617.33 to 616.58 mbsf), was deposited by the final settling of sediment resuspended and transported by tsunami and seiche waves (figs. S2 and S3) (*25*, *27*). Unit 1G is overlain by a ~3-cm-thick gray-green marlstone (616.58 to 616.55 mbsf) that transitions into the lowermost Danian pelagic white limestone (Unit 1F) (Figs. 2 and 3 and figs. S1 to S3) (*24*, *29*). The fine grain sizes of the transitional unit, from clay to fine silt, imply that most of this sediment was deposited through resuspension and settling as energy subsided in the Gulf of Mexico (*27*, *29*). Two intervals of soft sediment deformation in the middle and upper parts of the transitional unit attest to seismic disturbance and local mass wasting on the topographically high peak ring, at least before deposition of the overlying green marlstone (*25*). Yet, Site M0077 appears to have largely been shielded from major disturbances, possibly due to its location in a depression atop the peak ring (*23*–*25*, *27*, *29*).

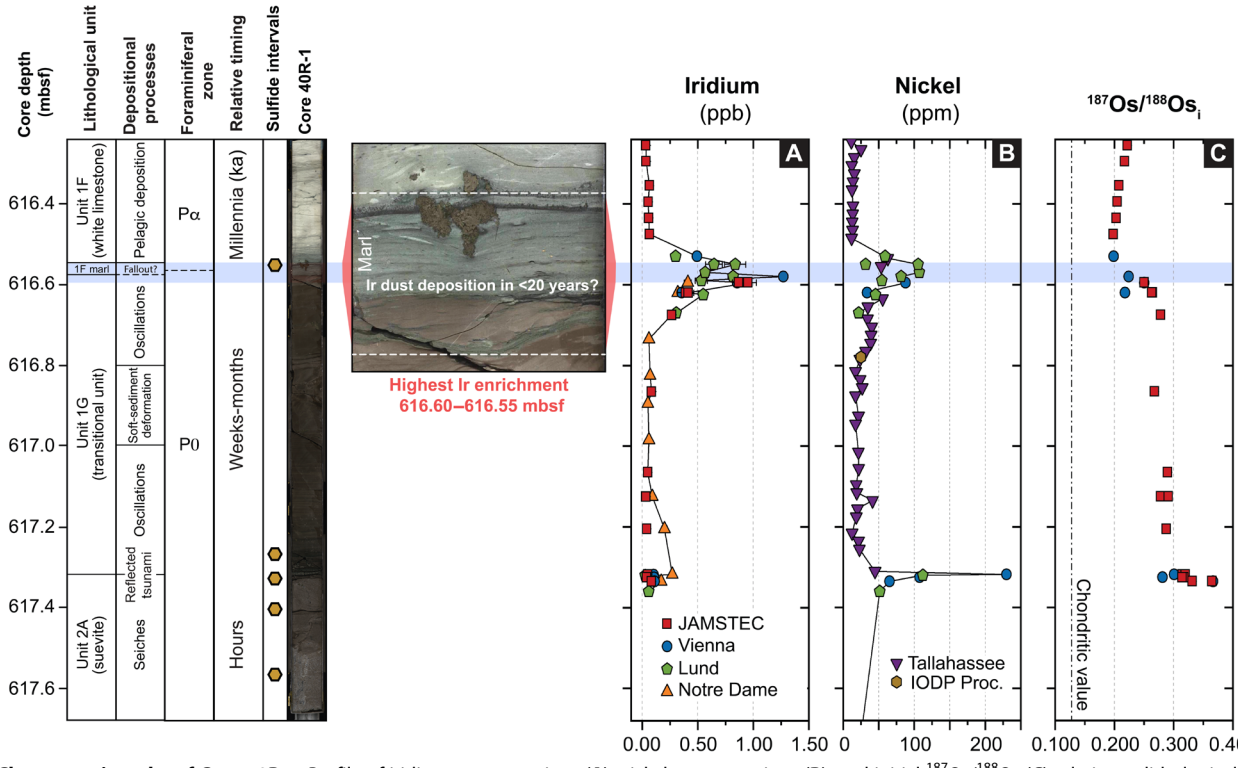

Fig. 3. Chemostratigraphy of Core 40R-1. Profile of iridium concentrations (**A**), nickel concentrations (**B**), and initial $^{187}Os/^{188}Os$ (**C**) relative to lithological units, proposed depositional mechanism, foraminiferal zone (*24*), relative timing after impact, and sulfide mineral intervals. Symbol legends designate the laboratories where the respective siderophile element concentrations were determined. Uncertainties on Ir concentrations and $^{187}Os/^{188}Os$ are expressed as 2 SE or 2σ for data determined by mass spectrometry and instrumental neutron activation analysis iridium coincidence spectrometry, respectively (mostly contained within the symbols). The interval of highest Ir enrichment is highlighted in blue, which corresponds to the white dashed lines in the enlarged core photograph. The high-resolution line scan photo is from the onshore science party (*23*). While the siderophile element enrichment in the gray-green marlstone and at the top of the transitional unit reflects the deposition of meteoritic matter, the elevated concentrations at the bottom of the transitional unit result from sulfide mineralization following hydrothermal activity in the impact basin. The highest HSE enrichment at the base of the gray-green marlstone (~616.58 mbsf) is interpreted to record the settling of Ir-rich dust, estimated to have been deposited within a few decades after the impact event, and subsequently reworked into a broader interval.

Siderophile element geochemistry and sulfide distribution

We first use a combination of moderately siderophile Ni and lithophile Cr concentrations as a proxy to trace possible enrichments in Ir and the other HSEs (*7*). Distinct Ni enrichments in excess of 100 ppm are observed both at the top and bottom of the transitional unit, compared to relatively low Ni concentrations (<35 ppm) in the rest of the transitional unit, the suevite (Units 2A, 2B, and 2C), impact melt rocks (Units 3A and 3B), and granitic basement (Unit 4) (Figs. 2 and 3). Just above a fairly sharp, stylolitized contact, the lowermost part of the transitional unit contains, spread over a few centimeter-thick interval (617.36 to 617.32 mbsf), several millimeter-thick layers that are enriched in Ni, with concentrations exceeding 200 ppm (fig. S3). At the top of the unit, a ~5-cm interval from 616.58 to 616.53 mbsf that includes the gray-green marlstone is characterized by Ni concentrations of 50 to 100 ppm (Fig. 3 and fig. S3). The elevated Ni concentrations at the bottom of the transitional unit (617.34 to 617.32 mbsf) are accompanied by the highest Re and Os concentrations in the measured profile but coincide with only modestly elevated Ir, Ru, and Pd contents. In contrast, the uppermost part of the transitional unit and the gray-green marlstone (616.63 to 616.53 mbsf) are characterized by Ir concentrations at least one order of magnitude higher than those of upper continental crust (Figs. 3 and 4 and fig. S4). On the basis of 49 bulk rock Ir measurements, the Ir values approximate ~1.0 parts per billion (ppb) over a ~5-cm interval from 616.60 to 616.55 mbsf. Only a single Ir data point at the base of the gray-green marlstone layer (~616.58 mbsf) exceeds 1 ppb and is associated with relatively high Os, Ru, Pt, and Pd concentrations (Figs. 3 and 4 and fig. S4). Initial Os isotope ratios ($^{187}Os/^{188}Os_i$) in the lowermost transitional unit range from 0.281 to 0.367 and decrease to 0.224 to 0.250 in the uppermost transitional unit and overlying gray-green marlstone. The $^{187}Os/^{188}Os_i$ drop even further to ~0.198 in the lowermost Danian white limestone of Unit 1F (616.53 to 616.48 mbsf), after which they slowly return to more radiogenic values of ~0.222 at 616.26 mbsf (Fig. 3). Whereas the HSEs elsewhere in Core 40R-1 display concentrations and signatures similar to those observed for the upper continental crust, following a tilted pattern with low Ir and Ru and higher Pt and Pd concentrations, the base of the gray-green marlstone and the top of the transitional unit exhibit HSE concentrations an order of magnitude higher than the upper continental crust with relatively flat CI chondrite–normalized HSE patterns (Fig. 4). All core intervals, with exception of those neighboring the gray-green marlstone (~616.63 to 616.53 mbsf), exhibit Ir and other HSE concentrations that are similar to those previously measured for the majority of the samples from the onshore drill sites Chicxulub 1 (C1), Yucatán 6 (Y6), and Yaxcopoil-1 (Yax-1) (Fig. 1), lacking clear meteoritic contributions

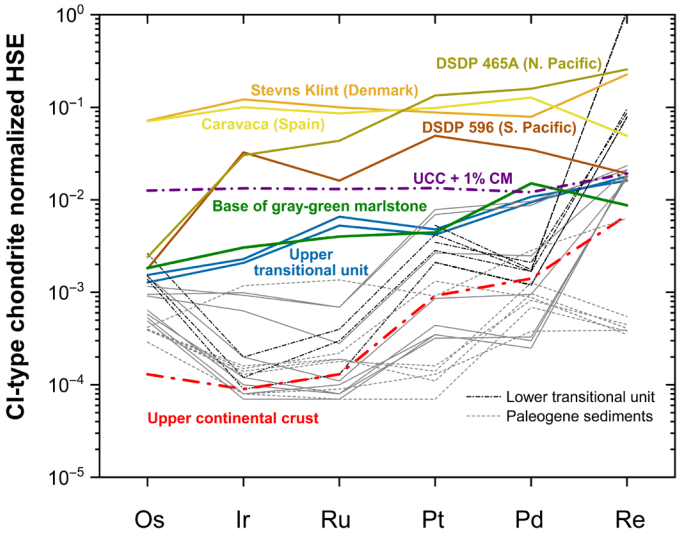

Fig. 4. Cl-Chondrite normalized HSE patterns. Green and blue lines denote samples from the base of the gray-green marlstone and at the top of the transitional unit (616.60 mbsf), respectively. Gray and black lines designate other intervals in Core 40R-1. For comparison, the admixture of 1% of CM carbonaceous chondrite to upper continental crust (UCC) was calculated and is shown in purple. HSE concentrations for CI and CM chondrites, UCC, and distal K-Pg boundary sections are from (*8*, *38*, *58*). The paleogeographic locations of the different K-Pg boundary sections shown here are highlighted in Fig. 1.

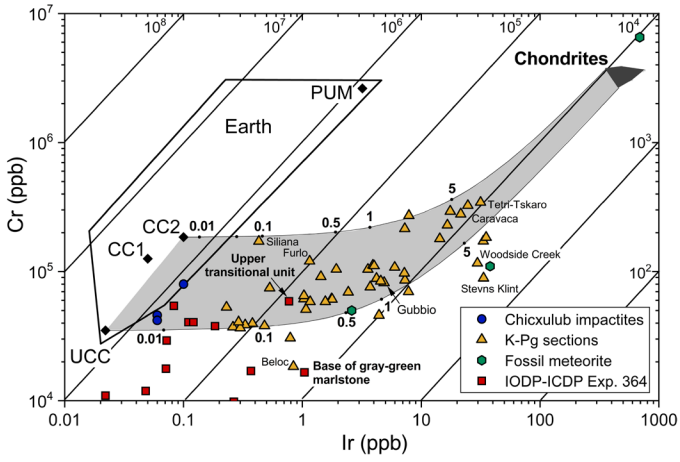

Fig. 5. Double logarithmic plot of Cr versus Ir concentrations. Data for global K-Pg sections (*7*), Chicxulub fossil meteorite fragments (*13*), Yaxcopoil-1 and Yucatán 6 suevite and impact melt rocks (*31*), and average data compiled for Core 40R-1 samples, compared to the Cr/Ir ratios in various terrestrial lithologies and chondrites. The gray field indicates mixing trajectories between chondritic projectiles and common terrestrial targets. CC, continental crust; PUM, primitive upper mantle [(*59*) and references therein].

and approximating continental crustal values. In general, Chicxulub impactites typically contain less than 0.1% of a chondritic component (Figs. 5 and 6) (*30*–*32*). A few powdered splits of impact melt rock from the Y6 and C1 drill cores represent the only exceptions, for which elevated Ir concentrations up to 15 ppb have previously been measured. The latter remain difficult to interpret based on their stratigraphic position but may represent atypical sample heterogeneity (*30*, *33*).

Cretaceous-Paleogene boundary layers across the globe are associated with sulfide minerals (*5*), which can host a wide range of chalcophile and siderophile elements [e.g., (*34*, *35*)]. However, secondary sulfide minerals (including pyrite, Ni-bearing pyrite, and chalcopyrite) are found throughout the IODP-ICDP Expedition 364 drill core and have largely been linked to hydrothermal processes (*36*). In Core 40R-1, sulfide grains and layers occur not only in the Ni enriched intervals both at the top and at the bottom of the transitional unit but also elsewhere (figs. S1 to S3) (*27*, *29*). These sulfides display variable mineralogy, composition, and size (table S1), with nodules up to a few centimeters disrupting the bedding in the transitional unit at ~616.7 mbsf and in the gray-green marlstone (Figs. 2 and 3 and fig. S1).

DISCUSSION

Identifying the global iridium layer at Site M0077

Compared to the millimeter- to centimeter-thick reddish K-Pg boundary clay layers at most distal sites (>5000 km from Chicxulub) that display a sharp Ir concentration peak across the boundary, K-Pg boundary event deposits closer to the crater (<1000 km) are considerably thicker, with up to 80-m-thick ejecta-rich deposits in Mexico (*3*, *5*, *6*). These deposits provide evidence for high-energy sediment transport and are typically accompanied by moderate Ir anomalies spread over a wider interval (Fig. 1) (*3*, *5*–*7*). Similarly, cores recovered close to the crater rim within the impact structure reveal >100-m-thick impact breccia sequences, with little to no Ir (*3*, *5*). In Core 40R-1 from Site M0077, the base of the gray-green marlstone displays a distinct Ir anomaly in excess of ~1.0 ppb, comparable in magnitude to those measured at the most proximal K-Pg boundary sites (e.g., 0.8 to 1.0 ppb Ir at Guayal, Tabasco, México, at Bochil, Chiapas, México, and at El Mimbral, Tamaulipas, México) (Figs. 1, 3, 4, and 5 and fig. S4) (*6*, *7*). These values are slightly lower than those measured for generally thinner distal K-Pg boundary sections (e.g., 4.9 to 8.0 ppb at Gubbio, Italy or 16.6 to 56 ppb at Caravaca, Spain) (*3*, *7*) yet significantly enriched relative to typical upper continental crustal values of ~0.04 ppb (Figs. 1, 4, and 5) (*8*). The dilution of the Ir signal in proximal sites and within the crater confirms that, although the effects of impact-induced seismic and margin collapse events may have been dampened locally, large volumes of sediments were transported within the Gulf of Mexico (*5*, *15*, *16*) and the Chicxulub crater after the impact (Fig. 5) (*27*). The Ir-rich interval in Core 40R-1 forms a relatively wide peak with concentrations >0.3 ppb over ~15 cm, yet only the base of the gray-green marlstone and uppermost transitional unit with the highest Ir, Ru, Pt, and Pd concentrations display near-chondritic interelement ratios (Fig. 4). In the interval from 616.62 to 616.58 mbsf, Os concentrations range from 0.426 to 0.824 ppb, with Os/Ir varying between 0.58 and 1.34, close to the chondritic ratio of ~1.1 (fig. S4). The initial Os isotope ratios ($^{187}Os/^{188}Os_i$) of 0.218 to 0.264 in this interval are within range of those typically found at marine K-Pg boundary sequences across the globe (0.161 to 0.230) (*14*) and imply a meteoritic contribution equivalent to ~0.1% CI chondrite (Fig. 6). The latter concurs with estimates based on the Cr and Ir concentrations (Fig. 5). The even lower $^{187}Os/^{188}Os_i$ of ~0.198 in the lowermost Danian white limestone of Unit 1F (616.53 to 616.48 mbsf) may denote a shift in the mode of Os delivery (Fig. 3). While Os likely first arrived in the form of particulate matter, the lower $^{187}Os/^{188}Os_i$ combined with considerably higher Os/Ir ratios in the lower Paleogene

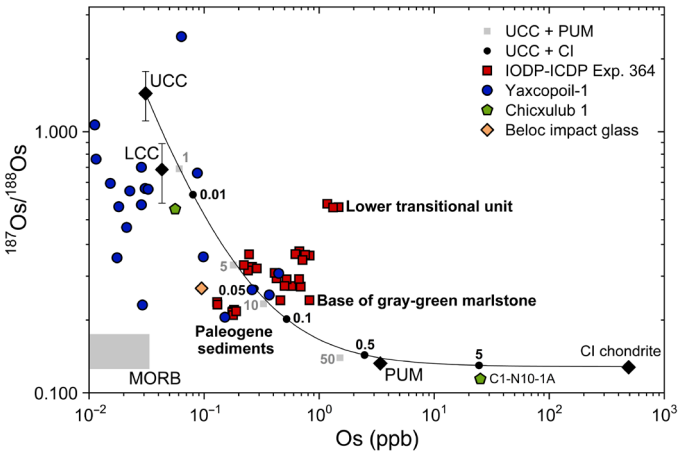

Fig. 6. Os isotope ratios versus Os concentrations. $^{187}Os/^{188}Os$, not corrected for radiogenic ingrowth, versus Os concentrations determined for the IODP-ICDP Expedition 364 Core 40R-1 samples, impact melt rocks, melt clasts, and lithic clasts from Yaxcopoil-1 (*32*), Chicxulub 1 impact melt rock (*30*), and Beloc impact glass (*30*). The curve represents the calculated mixing line between CI carbonaceous chondrite and the UCC, with admixture of up to 5% CI chondrite. The mixing trajectory between UCC and PUM is indicated by gray solid squares (1 to 50%). Because of low Re/Os ratios, chondritic materials typically yield unradiogenic $^{187}Os/^{188}Os$ ratios of ~0.13, with limited variation between different types of chondrites (*58*). Most samples of Core 40R-1 plot close to the mixing line between chondrite and UCC, similar to Yaxcopoil-1 impactites and Beloc impact glass. The highest meteoritic contribution of ~0.1% is measured at the base of the gray-green marlstone. The samples from the lower part of the transitional unit (downward from ~617.32 mbsf) plot to the right of this mixing line, as Os was likely concentrated through hydrothermal activity and sulfide mineralization. This plot is based on (*59*) and references therein.

white limestone of Unit 1F may indicate a larger admixture of vaporized unradiogenic meteoritic Os to the ambient seawater (*37*), possibly brought in from nearby land surfaces.

Similar to proximal sites, the Ir anomaly at Site M0077 is preceded by (now altered) vitric impact melt particles, often with filled vesicles, in the upper part of the suevite and transitional unit (fig. S5) (*27*, *29*). More rarely, a ~1.2-mm-sized impact spherule has also been found in the upper sorted and layered suevite (figs. S1 and S6). These impact spherules may have been part of the proximal Chicxulub impact glass ejecta transported back to the crater by resurge and seiches most likely through the morphological gap in the crater rim to the northeast (*19*, *27*). Similar to the Ir concentrations, the abundance and preservation of impact spherules depend on the distance from Chicxulub and the local depositional environment at the time of the impact (*5*). In the Gulf of Mexico and adjacent areas, the separation between coarse-grained impact spherules and subsequently deposited finer-grained HSE-rich ejecta phases has been used to suggest that the clastic K-Pg boundary deposits were deposited in an extremely brief period of time (*3*, *5*).

Reworking and hydrothermal overprint

Our results indicate that a meteoritic component consistent with a chondritic impactor dominates the siderophile element signatures in the gray-green marlstone interval of Core 40R-1 recovered from Site M0077 on the Chicxulub peak ring (Fig. 4). The highest Ir concentrations are found at the contact between the uppermost transitional unit and the base of the gray-green marlstone; however, this Ir anomaly is redistributed over a ~5- to 20-cm interval, across which there is a substantial change in sedimentary regime (Fig. 3). Postdepositional remobilization of siderophile elements is well documented at K-Pg boundary sites, including pelagic and hemipelagic sediment cores at distal sites, and generally results in redistribution of the HSE, typically over a few centimeters but, in extreme cases, up to several meters from the boundary (*38*). This redistribution, often with fractionation between the HSE, mostly results from reworking, diagenesis, bioturbation, and chemical diffusion (*7*). Changes in sedimentary redox conditions are known to variably redistribute the HSE (*39*), but no redox shifts consistent with the observed siderophile element distribution pattern are evident in Core 40R-1 (*40*). There is evidence for bedding distortion in Core 40R-1, in the form of soft-sediment deformation, burrowing in the upper ~15 cm of the transitional unit, wood, and charcoal fragments indicating waves entering the crater and local down-warping of laminae due to early diagenetic pyrite growth in the gray-green marlstone (fig. S1) (*25*, *27*, *29*). However, while the transition between the upper transitional unit and the gray-green marlstone of Unit 1F may contain minor hiatuses, there is no evidence for a gap in deposition (*25*). This continuity is supported by the fine micrite of the gray-green marlstone that resembles that of the transitional unit but is distinct from micrite in the overlying white limestone (*29*). Evidence of substantial mass wasting is also lacking and restricted only to the underlying suevite intervals (*23*, *25*, *27*, *29*). Overall, the Ir anomaly appears largely to have been preserved in place but was broadened as the result of various postdepositional processes.

Impact heating and deformation generate porous and permeable rocks that following the input of water and driven by a hot central melt sheet led to a pervasive hydrothermal system at Chicxulub (*36*). The drill core recovered by IODP-ICDP Expedition 364 displays widespread evidence for the effects of an extensive hydrothermal system that was initially hot (>300°C) and subsequently cooled to produce a series of lower-temperature minerals. Among the various hydrothermal minerals and mineral assemblages encountered in the granitoid and suevite intervals of the drill core (Core 40R and deeper), secondary sulfides are common, strongly affecting the observed siderophile and chalcophile element distribution (*36*). Crucial to Core 40R-1, sulfide mineralization occurs both near the top and bottom of the transitional unit (Figs. 2 and 3 and figs. S2 and S3) (*29*). Pyrite in all intervals is preserved as 5- to 100-μm rhombic and hexagonal sheet-like crystals and as 10- to 75-μm-long blade-like crystals (figs. S5 and S7) (*29*). The lowermost transitional unit contains several distinct layers of pyrite and other associated sulfide minerals (figs. S2 to S5 and S7 to S11), with the highest Ni enrichment of Core 40R-1 at 617.32 mbsf. Specific sulfide mineralization, such as $NiCoFeS_2$, occurs in the suevite and transitional unit and hints at black smoker-like venting of hydrothermal fluids into the post-impact Chicxulub basin (see the Supplementary Materials). Pronounced Co, Te, and Tl concentrations in pyrite imply precipitation from fluids that penetrated the buried sediment column at high temperatures (possibly up to ~350°C) (fig. S8), while the chemical compositions of most sulfide mineral grains confirm a mostly continental crustal derivation (fig. S9).

The gray-green marlstone at the top of the transitional unit also includes a pyritic interval at ~616.55 mbsf with two thin concentrated layers as well as large (centimeter-sized) nodules. Sulfide minerals at the top of the transitional unit are dominated by chondritic Ni/Co ratios and enriched in chalcophile elements such as As and Sb

(figs. S8 to S10). At anoxic marine K-Pg sites, pyrite is also often enriched in As and Sb and interpreted to reflect formation by anaerobic bacteria during early diagenesis (*34*). Microbially formed framboid pyrite has also been reported from the suevite units and is associated with bacterial sulfate reduction (*36*). However, the distinct composition and size of the pyrite grains and layers at the top of the transitional unit infer formation under a different temperature regime during which accessible meteoritic matter was scavenged (figs. S8 and S9). A first generation of sulfides, formed at elevated temperature (>250°C) from hydrothermal fluids, was followed by the formation of early diagenetic pyrite at considerably lower temperatures, as commonly found at anoxic K-Pg boundary sites (*5*). The hydrothermal system at Chicxulub with initial temperatures of 300° to 400°C persisted in excess of 10^5 years (*36*), long after normal hemipelagic deposition resumed. The siderophile element enrichments in Ni, Os, Re, and Pt at the bottom of the transitional unit thus reveal hydrothermal redistribution of deep crustal and possibly meteoritic components, while the distribution of other HSEs (e.g., Ir, Ru, and Pd) was not affected by substantial remobilization as the result of the hydrothermal system (Figs. 3 to 6 and fig. S4).

Iridium fluence

As the Ir enrichment largely remained in place following initial deposition, we conservatively estimate the total Ir fluence at Site M0077 to be ~20 ng Ir/cm^2, assuming an average sediment dry density of 2.53 g/cm^3 (*41*) and background Ir concentration of 50 ppt (Figs. 3 and 4). Sites close to or within the crater have a lower total Ir fluence at 10 to 45 ng/cm^2 (*6*, *7*, *20*, *42*) compared with a mean global Ir fluence of 55 ± 3 ng/cm^2, calculated on the basis of 52 marine and nonmarine sections (*42*). Microkrystite spherules, together with the spinel crystals these contain, are known to hold a substantial fraction of impactor material, but their chemistry and distribution pattern between K-Pg boundary sites display a large asymmetry across the globe (*5*, *11*). Iridium concentrations are highest in the spinel-bearing spherules (up to >100 ppb) and lower in the nonspinel bearing spherules and surrounding clay (1 to 10 ppb) (*11*, *14*, *43*). Rocchia *et al.* (*43*) reported a strong correlation between the location of spinel crystals and the Ir anomaly and concluded that the Ir was associated with the spinel and had remained in situ since deposition, whereas Ir in the surrounding clay was more mobile. At Site M0077, microkrystite spherules and magnesioferrite spinel crystals, known to be particularly resistant to weathering (*11*, *43*), have not been found so far. Microkrystite spherules form a volumetrically significant component of the K-Pg layer at distal sites, with up to 20,000 spherules/cm^2 and an average spherule diameter of 250 μm (*5*). Mass balance considerations indicate that these spinel-bearing spherules contribute a considerable fraction, up to 80%, of the Ir budget at distal K-Pg boundary sites. On the basis of Core 40R-1, this may not be a global phenomenon but may rather be linked to the carrier phases in the K-Pg HSE layer, which may be different between distal and more proximal sites.

HSE carrier phase and fallout of dust

Despite the association of various chalcophile and siderophile elements with sulfide minerals, the interval with the highest Ir enrichment from 616.60 to 616.55 mbsf stretches beyond the pyritic interval and the transition from the top of the transitional unit to the gray-green marlstone. Moreover, no single lithology or mineral phase can be resolved that is associated with the Ir-enriched interval. Given the lack of any obvious Ir carrier phase and occurrence of HSEs in discrete nuggets (figs. S10 and S11), Ir and the other HSEs were likely transported through and settled from the atmosphere as microscopic dust. As the base of the gray-green marlstone at ~616.58 mbsf contains the highest HSE concentrations in near-chondritic interelement ratios, this interval likely represents the level of first Ir dust deposition, from which the HSE were redistributed into the uppermost transitional unit and overlying gray-green marlstone (Fig. 3). The nanometric size of Ir-bearing metal nuggets condensed from the vaporized ejecta has previously been suggested [(*11*) and references therein] and is consistent with the enormous volume of dust produced following impact on volatile-rich targets (*1*, *12*). The stratigraphic level where the impact-related dust settled out and subsequently altered to clay (*1*, *11*) coincides with the appearance of possibly atmosphere-derived charcoal-bearing layers near the level of the gray-green marlstone (*27*), as well as 40- to 100-μm altered vitric impact melt particles and fine carbonate dust immediately below these upper charcoal-bearing layers (fig. S1) (*29*). After rapid deposition of most sediments of the transitional unit by tsunami and seiche waves due to continued seismic and mass wasting events within the Gulf of Mexico and internal to the crater (*25*), energy eventually dissipated and sedimentation slowed down, allowing the deposition of atmospheric fallout at the base of the thin hemipelagic gray-green marlstone unit. While minor redeposition of the settled dust cannot be dismissed, there are indications for continuity in sedimentation between the transitional unit and gray-green marlstone, confirming the overall rapid deposition of the transitional unit and underlying layers. However, the transition to the green-gray marlstone represents a notable change in sedimentation rate, with the deposition of the entire ~3-cm marlstone interval transpiring over a considerably longer period of time (Fig. 3 and fig. S1).

Timing of the deposition

If the near-chondritic HSE signature at the base of the gray-green marlstone results from the primary settling of atmospheric fallout of fine extraterrestrial material, then this places critical time constraints on the deposition of the transitional unit and underlying units (Fig. 3). While Ir carried by microkrystites was deposited at K-Pg boundary sites within several hours to a few days after the impact event, Ir that was part of the fine-grained material in the dust cloud was likely deposited over a more extended period of time, potentially circling Earth in the atmosphere for up to a few years after the impact and then taking up to a couple of decades (<20 years) to be deposited. This shortest possible timing is inferred from hydrocode modeling (*12*) and considerations based on Stokes' and Newtonian laws (see the Supplementary Materials). If the highest Ir concentration in the profile reflects the temporal horizon during which this globally distributed impactor-rich dust settled, then the majority of the transitional unit was deposited within weeks to a few years after the impact. This is in accordance with the dominant depositional patterns in the upper suevite and the transitional unit that indicate rapid sedimentation characterized by graded bedding, local cross bedding, and evidence of oscillatory currents (*25*) and the settling through the water column of impact-related materials in the gray-green marlstone, particularly charcoal and woody material (*29*). However, note that minor effects from aftershocks, continental margin collapse events, and post-impact storms may have kept Ir and the other HSE mobile in the environment for several hundreds to thousands of years after the initial deposition (*3*, *5*, *7*).

The timing of the entire gray-green marlstone interval is more challenging to resolve. While rapid deposition for the majority of the transitional unit was first suggested on the basis of ^{3}He measurements and Stokes' law calculations, the occurrence of earliest Paleocene planktic foraminifera in the gray-green marlstone at least down to 616.57 mbsf places an upper limit of 30 ka post-impact (*24*). Additional ^{3}He isotope measurements confirm a substantial slowdown in sedimentation rates in the uppermost 15 cm of the transitional unit (*29*), in agreement with the occurrence of multiple layers possibly redeposited by a series of distal gravity flows and burrows down to ~20 cm into the transitional unit that could suggest deposition over a period of decades to centuries (*44*). If the ~3-cm gray-green marl unit was deposited at pelagic-like rates for the Danian of ~0.5 cm/ka (*5*, *15*), then the entire gray-green marlstone layer may have taken up to ~6000 years to deposit. Faster rates remain possible if the sediment was remobilized over a large area or if a large fraction of the sediment is reworked Cretaceous carbonate mud. However, this timing needs to be reconciled with the lowermost occurrence of *Parvularugoglobigerina eugubina* and other Paleocene planktic foraminifera at 616.56 to 616.57 mbsf (*24*, *29*) that defines the boundary between foraminiferal zones P0 and Pα. This zonal boundary is estimated to occur as much as 30 ka (*9*) and as little as 4 to 16 ka (*5*), or even 3 ka (*15*), after the impact. Very slow sedimentation at the top of the transitional unit, with a brief P0 interval, reconciles the co-occurrence of the Ir anomaly with the lowermost occurrence of Paleocene planktic foraminifera in the gray-green marlstone, especially when considering the effects of Ir diffusion and reworking in the sedimentary column. Taking into account variable sedimentation rates, mixing of impactor-derived dust and foraminifera, pyrite growth, bioturbation, and centimeter-scale upward remobilization of Ir, the entire gray-green marlstone interval may have taken up to a few millennia to deposit.

Implications for the return of life

Both microfossils and biomarkers indicate that life returned to the Chicxulub crater in the immediate aftermath of the impact (*24*, *29*, *40*). The water column above the sampled peak-ring location likely became habitable within days to months after the impact with survivor nanoplankton and a monospecific, red tide–like dinoflagellate assemblage arriving in the aftermath of the tsunami waves, possibly fueled by the input of terrigenous nutrients (*29*). The earliest Danian nanoplankton and dinocysts occur in the seiche layers of the lower transitional unit. The diversity of phytoplankton dropped at the base of the hemipelagic gray-green marlstone (*24*, *29*), where the impactor-rich dust appears to have settled. A nearly monogeneric calcareous dinoflagellate resting cyst assemblage indicates that calcareous phytoplankton were experiencing harsh surface ocean conditions in the nascent impact crater, while coexisting planktic foraminifera were diverse and abundant, indicating a recovering zooplankton community (fig. S1) (*24*, *29*). Within the gray-green marlstone, microbial biomarkers indicate a thriving bacterial community, which may have been adapted to low-light conditions and/or supported by nutrients and heat from hydrothermal activity (*40*), while a diverse assemblage of planktic and benthic foraminifera (*24*), possible crustaceans, larval fish and coprolites (*29*), and microbenthic trace makers is also present (*45*). The rapid adaptation of life to the early Chicxulub crater demonstrates a fast return to low-energy environments in the crater and a resiliency of life under extraordinarily harsh conditions. Impact craters such as Chicxulub thus provide unique habitats for life, which may also have been present on the early Earth (*46*).

The first unambiguous detection of a well-characterized positive Ir anomaly within the Chicxulub crater itself represents the closest and strongest temporal and spatial connection between the formation of the impact structure and the global K-Pg boundary sequences so far. The preservation of the Ir anomaly within the Chicxulub structure may be rare, given the energetic environment of tsunamis and seiches following the impact event. This implies that most of the energetic activity had ceased before Ir settled to the crater peak ring and floor. Similarly, the extent of recorded post-impact hydrothermal activity (*36*) implies the dissolution that carried chalcophile and siderophile elements to the seafloor took place in deeper core intervals, and while those fluids vented to the surface, they essentially breached through the Ir layer without substantially modifying it. As a result, the IODP-ICDP Expedition 364 core contains an exceptionally detailed record of the impact and post-impact processes associated with the formation of the Chicxulub crater. The clear association of the Ir anomaly within the Chicxulub impact structure and the recorded biotic response confirms the direct relationship between the impact event and the K-Pg mass extinction.

MATERIALS AND METHODS

Materials

In 2016, the IODP and the ICDP jointly drilled the 1335-m deep Site M0077 into the Chicxulub peak ring offshore of the Yucatán Peninsula and successfully recovered a continuous core from 505.7 to 1334.7 mbsf (*22*) using the lift boat *L/B Myrtle* (*23*). The core was logged and sampled at the MARUM Center for Marine Environmental Sciences, University of Bremen, Germany. Initial geochemical and mineralogical characterization at MARUM (*23*) included core photography, spatially resolved and discrete bulk x-ray fluorescence spectrometry (XRF), XRF line scanning, determination of total carbon and sulfur content using elemental analyzers, and x-ray diffraction analysis. These analyses encompassed Core 40R-1 and enabled a first examination of this key succession that represents the transition from the upper suevite interval (Unit 2A) to the post-impact sedimentary rocks (Units 1G and 1F).

On the basis of these first results, bulk samples throughout the core section that exhibited chalcophile and siderophile enrichments were selected, and these were analyzed for major and trace element concentrations, using inductively coupled plasma mass spectrometry (ICP-MS) and instrumental neutron activation analysis (INAA). Focus was placed on the analysis of HSE concentrations (Os, Ir, Ru, Pt, Pd, and Re) using isotope dilution ICP-MS as well as INAA iridium coincidence spectrometry (ICS). Osmium isotope ratios (^{187}Os/^{188}Os) were determined for a smaller subset of samples using negative thermal ionization mass spectrometry (N-TIMS). In total, 49 samples were measured for iridium concentrations by four independent laboratories, resulting in a uniquely detailed profile (Fig. 3). In addition, four discrete core sections at 616.54 to 616.60, 616.62 to 616.68, 617.30 to 617.34, and 617.35 to 617.37 mbsf, sampling Units 2A, 1G, and 1F, and their transitions were subjected to μXRF [two-dimensional (2D) maps] and laser ablation (LA)–ICP-MS analysis. Thin sections borrowed from the core library and thick sections produced from the available samples were studied using optical microscopy and scanning electron microscopy (SEM). Sulfide minerals from the gray-green marlstone, lower transitional unit, and uppermost suevite sections

were analyzed using electron microprobe analysis (EMPA) and LA-ICP-MS.

Methods

μXRF at Vrije Universiteit Brussel

High-resolution elemental abundance maps of the cut and lightly polished surface of four discrete core sections at 616.54 to 616.60, 616.62 to 616.68, 617.30 to 617.34, and 617.35 to 617.37 mbsf were obtained using the Tornado M4 μXRF scanner (Bruker Nano GmbH, Berlin, Germany) at the Vrije Universiteit Brussel. μXRF mapping was carried out under near-vacuum conditions (20 mbar), along a 2D grid with 25-μm spacing, a spot size of 25 μm, and an integration time of 1 ms per pixel. The Rh x-ray source was operated under maximum energy settings (600 μA, 50 kV), and no source filters were applied. This mapping approach by μXRF permits qualitative to semiquantitative element abundance distributions to be visualized (Fig. 2 and figs. S2 and S3).

EMPA at ASU and NASA-JSC

X-ray intensity mapping and quantitative wavelength-dispersive spectrometry (WDS) analyses at Arizona State University (ASU) were done using a JEOL JXA-8530F field emission electron microprobe at ASU's Eyring Materials Center. For x-ray mapping, a focused beam with an accelerating voltage of 20 kV and a beam current of 10 nA was used. The 200 × 200 pixel maps were acquired via beam deflection with a dwell time of 50 ms per pixel. WDS analyses were done using a 1-μm beam diameter at an accelerating voltage of 20 kV and a beam current of 20 nA. Count times on the peaks and backgrounds were 60 s for the Kα lines of Si, Mg, Fe, Zn, and Cu, 100 s for the Kα peaks of Co and Ni, 80 s for the Kα line of S, and 120 s for the Lα line of Cd. Detection limits were 0.01 weight % (wt %) for Si, Co, and Ni, 0.02 wt % for Mg and S, 0.03 wt % for Fe, 0.04 wt % for Zn and Cu, and 0.07 wt % for Cd. Calibration standards used were pure metals for Cd, Co, Cu, and Ni, troilite for Fe, synthetic ZnS for Zn and S, and San Carlos olivine for Mg and Si. A correction was applied for the peak overlap of the Fe Kβ line with the Co Kα line. All WDS data were processed with Probe for EPMA by Probe Software Inc.

At the NASA Johnson Space Center (NASA-JSC) in Houston, analytical EMPA was conducted on polished thin sections by WDS using a CAMECA SX-100 microprobe equipped with five spectrometers [see also results in (*36*)]. Sulfide minerals were analyzed at an accelerating voltage of 15 kV, a beam current of 20 nA, and a beam diameter of 1 μm. Mineral standards used for EMPA included Canyon Diablo troilite for Fe and S; pentlandite for Ni; cobalt metal for Co; copper metal for Cu; willemite for Zn; diopside ($En_{73}Fs_{16}Wo_{11}$) for Si; labradorite ($An_{56}Ab_{42}Or_2$) for Ca; oligoclase ($Ab_{75}An_{21}Or_4$) for Na; and orthoclase ($Or_{90}Ab_{10}$) for K. To reduce the effects of beam-induced volatilization, Na and K were analyzed first on each spectrometer. Dwell times were 20 s on element peaks, 30 s for Ni and Co, and half of the peak counting time on backgrounds adjacent to peaks. Electron microprobe results were corrected for the spectral interference Co Kα/Fe Kβ using a Co-free iron metal standard. Reported EMPA results meet the criteria of standard calibration with an SD of ≤1%, reproducible standard-as-unknown compositions close to or within error equal to published values and, ideally, totals of ca. 100 ± 1 wt %. The detection limit for EMPA WDS analyses is typically ~0.01 wt %. All WDS results are presented in table S1 and figs. S5 and S7.

ICP-MS at Florida State University

Bulk samples (n = 39) were first powdered using a trace metal-clean ceramic ball-mill. Approximately 200 mg of powdered sample was weighed into trace metal-clean Savillex vials. Nitric acid (7 M HNO_3) was added to all samples until effervescence ceased, after which the mixtures were dried down. Then, 6 ml of concentrated HCl, HNO_3, and deionized water (at 1:1:2 ratio) was added to the clean Teflon vials, after which these were reacted in a CEM Mars 5 microwave digestion unit at 180°C to dissolve organic material. Samples were transferred to the previous Teflon vials for complete dissolution using mixtures of concentrated HF (hydrofluoric acid), HNO_3, and HCl. All acids used were distilled in-house and are better than trace metal grade acids and diluted using deionized water (18.2 megohm·cm). Elemental concentrations were determined versus an external calibration curve using an Agilent 7500cs quadrupole–based ICP-MS housed at the National High Magnetic Field Laboratory in the Geochemistry Group at Florida State University. United States Geological Survey (USGS) reference materials Devonian Ohio Shale (SDO-1) and Cody shale (SCo-1) were digested and analyzed along with the samples, and all reported values are at or better than 5% of the reference values. Procedural blanks were below detection limits. All results are summarized in table S2, while Cr and Ni concentration data are used in Figs. 3 and 5.

INAA at the University of Vienna

INAA was conducted on five samples from drill core intervals 616.59 to 616.60, 616.605 to 616.63, 617.315 to 617.32, 617.32 to 617.33, and 617.33 to 617.34 mbsf. The homogenized sample powders for these intervals were also used for $^{187}Os/^{188}Os$ and HSE concentration determination. Selected major (Na, K, and Fe) and trace element concentrations were determined by INAA (table S3). Representative subsamples of approximately 150 mg were sealed in small polyethylene vials and irradiated in the 250 kW Triga Mark-II reactor at the Atominstitut (TU Wien, Austria). After a cooling period of up to 5 days, the subsamples, together with international geological reference materials including the carbonaceous chondrite Allende (Smithsonian Institution, Washington DC, USA), the Ailsa Craig granite AC-E (Centre de Recherche Petrographique et Gechimique, Nancy, France), and the Devonian Ohio shale SDO-1 (USGS), were measured in three counting cycles, according to the half-lives of the nuclides in the Gamma Spectrometry Laboratory of the Department of Lithospheric Research, University of Vienna. Details on the instrumentation, method, accuracy, and precision are provided in (*47*) and references therein.

LA-ICP-MS at Ghent University

Spatially resolved LA-ICP-MS profiles were obtained across the intervals of interest following the procedures outlined in (*48*). The concentrations for 57 major and trace elements were determined by drilling lines-of-spots 50 μm in diameter using a 193-nm ArF* excimer–based Analyte G2 LA system (Teledyne CETAC Technologies, Omaha, USA), coupled to an Element XR (Thermo Fisher Scientific, Bremen, Germany) sector-field ICP-MS unit. This resulted in total profile lengths of ~4.48, ~1.95, ~5.61, and ~1.69 cm for the 616.55 to 616.59, 616.62 to 616.64, 617.29 to 617.34, and 617.35 to 617.37 mbsf sections, respectively (data S1). Individual data points were averaged per three to avoid nugget effects and analytical noise, leading to 853 data points at a lateral resolution of 150 μm (figs. S10 and S11). The sample and reference materials were mounted in a low-dispersion Cobalt ablation cell (Teledyne CETAC Technologies, Omaha, USA), while all other parameters were kept the same as in (*48*). The He carrier gas (0.5 liters/min) was mixed with Ar make-up gas downstream of the ablation cell using polyether ether ketone tubing (1-mm internal diameter) and a glass T-piece (5-mm

internal diameter) and introduced into the ICP-MS unit, operated at low mass resolution. Following preablation, analysis was performed via laser drilling using 50-μm circle laser spots, a laser dwell time of 24 s, a repetition rate of 25 Hz, and a beam energy density of 3.58 J/cm^2. Following conventional tuning (Th/U ~ 1, UO/U < 0.15%) using standard reference material NIST612 of the National Institute of Standards and Technology, precise and accurate trace element concentration data were obtained on the basis of external calibration, using a combination of MPI-DING and USGS glass reference materials ATHO-G, BHVO-2G, GOR 128-G, GOR 132-G, GSD-1G, GSE-1G, KL2-G, ML3B-G, StHS6/80-G, and T1-G and total oxide normalization to 100 wt %. The HDIP software (Teledyne CETAC Technologies, Omaha, USA) was used to background-correct the obtained data and integrate the signal intervals when the laser was fired. Following this procedure, precise and accurate major, minor, and trace element concentrations were obtained for USGS glass reference materials BCR-2G and BIR-1G. The average bias between reference value and experimentally obtained value is typically <10%. On the basis of the analyses of the reference materials, the reproducibility for the elements measured is 5 to 10% relative standard deviation (RSD) depending on the concentration. However, the HSE Re, Ir, Pt, and Au display precision above 20% RSD because of their occurrence at parts per billion–level concentrations only.

In addition, analysis of sulfide minerals was carried out using continuous LA-ICP-MS line scans with the Analyte G2 ArF* excimer–based LA system (Teledyne Photon Machines, Bozeman, USA) coupled to a Thermo XSeries 2 (Thermo Fisher Scientific, Bremen, Germany) quadrupole–based ICP-MS unit. Time-resolved LA-ICP-MS spectra for sulfide minerals from three core intervals, from 616.54 to 616.60 mbsf (gray-green marlstone and top of the transitional unit), from 617.30 to 617.34 mbsf (bottom of transitional unit), and from 617.35 to 617.37 mbsf (uppermost suevite), were collected (figs. S8 and S9). In addition to the reference materials mentioned above, a natural pyrite and sulfide pellet MASS-1 of the USGS were used for calibration purposes.

INAA ICS at Lund University

Following the LA analysis, the four discrete core sections at 616.54 to 616.60, 616.62 to 616.68, 617.30 to 617.34, and 617.35 to 617.37 mbsf were subsampled and powdered manually using a dedicated agate mortar and pestle. Ten samples in total (including one replicate) were analyzed for Ir, Co, Sc, Cs, Hf, Sb, and Ni using the triple coincidence iridium spectrometer at the Nuclear Physics Division, Lund University (table S4). This methodology represents an elaboration of the Luis W. Alvarez Iridium Coincidence Spectrometer built at the Lawrence Berkeley Laboratory in the 1980s (*49*), and additional details on the methodology can be found in (*50*).

Typically, 100 to 200 mg of sample mass is sealed in Heraeus Suprasil quartz ampullas. The ampullas are irradiated at the Hoger Onderwijs Reactor in Delft, in the Netherlands. The samples were irradiated for 18 hours with a thermal neutron flux of 2.5×10^{13} n cm^{-2} s^{-1}. Two in-house reference materials of DINO-1 (*49*) were included with the samples, one in each layer of the irradiation container. The selected detector material for the spectrometer is $LaBr_3$, a crystal with good energy (3%) at 662 keV (^{137}Cs) and time (subnanosecond) resolution, albeit not in range of the energy resolution achieved with a high-purity germanium (HPGe) detector. The detector system is constructed out of 14 detector elements of 31 mm × 31 mm × 78 mm (crystal size, 25 mm × 25 mm × 38 mm) arranged in such a way that the solid angle covered is close to 4π. The detectors are arranged cylindrically in two rings, each composed of six detectors with an additional detector at each end. Around the cylinder, six plastic scintillators are arranged for Compton suppression, i.e., background reduction. The light from the detector crystals is converted to electrical pulses via photomultiplier tubes and further amplified in a shaper (Mesytec MCFD-16) before the signals are digitized in a VERSAModule Eurocard (VME) analog-to-digital convertor. The shaper subsequently also extracts time information for each module, which is digitized by a VME time-to-digital convertor. The Mesytec module is also responsible for the logics of the system trigger. For the current dataset, the triggers are either signals in three of the detector modules or alternatively in two but then scaled down by a factor of 10. The data are stored in list mode for later evaluation, although most of the data are analyzed directly online. All data are normalized to the DINO-1 reference material analyzed in parallel to the samples throughout the process. In this way, the effect of neutron flux and exact irradiation time is eliminated.

Isotope dilution mass spectrometry at Japan Agency for Marine-Earth Science and Technology

HSE (Os, Ir, Ru, Pt, Pd, and Re) concentrations and Re-Os isotopic compositions for 22 samples (with six replicates) of Core 40R-1, including six Paleogene limestone samples, were determined by isotope dilution mass spectrometry after quartz glass tube digestion (table S5). The methods used for sample digestion, chemical purification, and mass spectrometry were based on procedures outlined in (*51*). Powdered samples (0.1 to 0.5 g) and spike solutions enriched in ^{185}Re and mixed ^{190}Os-^{191}Ir-^{99}Ru-^{196}Pt-^{105}Pd were transferred into a quartz tube. After adding 2 to 3 ml of inverse aqua regia, each quartz tube was frozen in a mixture of ethanol and dry ice, sealed with an oxygen-propane torch, and placed in an oven at 240°C for 72 hours. In between 0.5 and 3.0 ml of 38%, HF was added to the residual solids for desilicification (*51*).

Isotope ratio measurements of HSE were conducted using two types of mass spectrometers. Osmium concentrations and isotopic compositions were determined by N-TIMS (Thermo Triton Plus) at JAMSTEC, Japan. Osmium purified after CCl_4 solvent extraction and microdistillation was loaded in HBr on baked 99.997% Alfa Aesar Pt wire and covered with a NaOH-Ba(OH)$_2$ activator solution. The average total procedural blank for Os was 0.3 ± 0.1 pg (n = 16, 1 SD) with a ^{187}Os/^{188}Os ratio of 0.1503 ± 0.0139. Blank corrections were applied to all analyses individually rather than using a long-term average, as the blank values relate to each batch of digestion. The uncertainties for ^{187}Re/^{188}Os and ^{187}Os/^{188}Os were estimated by error propagation of the blank uncertainties. The average blank contributions to the measured Os concentrations and ^{187}Os/^{188}Os ratios of samples from the transitional unit were 0.28 and 0.14%, respectively. Those for the Paleogene limestone were 0.17% for Os and 0.05% for ^{187}Os/^{188}Os. All other HSE concentrations were determined using the Thermo Element XR HR-ICP-MS housed at the University of Tokyo in Komaba. Sample and standard solutions were interspersed throughout the analytical sessions to monitor and correct for instrumental fractionation. The nuclides monitored are ^{89}Y, ^{90}Zr, ^{95}Mo, ^{97}Mo, ^{99}Ru, ^{100}Ru, ^{101}Ru, ^{105}Pd, ^{106}Pd, ^{108}Pd, ^{111}Cd, ^{178}Hf, ^{185}Re, ^{187}Re, ^{191}Ir, ^{193}Ir, ^{194}Pt, ^{195}Pt, ^{196}Pt, and ^{202}Hg. Although all raw signal intensities were mathematically corrected for isobaric oxide interferences, contributions of interferences to analyte signals are mostly insignificant (<0.1%). The average total procedural blanks for the analyzed elements are 2.2 ± 1.2 pg for Ir, 2.9 ± 2.7 pg for Ru,

18.3 ± 7.1 pg for Pt, 7.9 ± 4.8 pg for Pd, and 1.2 ± 0.4 pg for Re (n = 16, 1 SD). As in the case of Os, all analyses were blank-corrected. Average blank contributions to samples from the transitional unit for Ir, Ru, Pt, Pd, and Re were 10, 3.4, 4.3, 3.5, and 0.37%, respectively, whereas average blank contributions to samples from the Paleogene limestone were 11% for Ir, 3.2% for Ru, 29% for Pt, 1.8% for Pd, and 15% for Re. The uncertainties on each sample were estimated by error propagation of the analytical uncertainties during ICP-MS measurement (2 SE) and blank correction. The accuracy of the analytical methods was evaluated by measuring a basaltic reference material. Five replicates of BIR-1a display excellent reproducibility (0.4% RSD for $^{187}Os/^{188}Os$, 8.6% RSD for Os, 8.0% RSD for Ir, 4.0% RSD for Ru, 3.8% RSD for Pt, 2.7% RSD for Pd, and 1.2% RSD for Re in the case of ~0.5 g subsamples; n = 5) and are in excellent agreement with previously published values of (*51*) for larger subsample masses of ~1 g. The applied analytical protocol is thus suitable for small amounts of sample.

Isotope dilution mass spectrometry at the University of Vienna and collaborating institutes

Seven sample powders, of which five were first characterized for major and trace element concentrations (table S3), with a weight between 0.06 and 0.5 g, were spiked with a mixed tracer composed of ^{185}Re, ^{190}Os, ^{191}Ir, and ^{194}Pt isotopes and digested in 7.5 ml of inverse aqua regia (HNO_3:HCl at 2:1 ratio) at 250°C and >100 bar in an Anton-Paar high-pressure asher for 12 hours. Details on the methods used for sample digestion, chemical purification, and mass spectrometry can be found in (*52*) and references therein. After digestion, Os was separated from the other HSE using a $CHCl_3$/HBr solvent extraction procedure. Osmium was further purified using a H_2SO_4/H_2CrO_4 microdistillation technique. The remaining aqua regia fraction was processed over anion columns (AG a-X8, 200 to 400 mesh) for removal of the matrix. Subsequent to column separation, cuts containing the HSE were dried down and redissolved in 0.5 M HCl for Ir, Pt, and Re. The $^{187}Os/^{188}Os$ ratios and the Os concentrations were determined at the Department of Lithospheric Research at the University of Vienna (Austria) using a ThermoFinnigan Triton TIMS operating in negative mode. Osmium was loaded as a bromide on Pt ribbon filaments covered with $Na(OH)/Ba(OH)_2$ activator. The runs were performed with an oxygen bleed to raise ionization yields. Osmium was measured as the OsO_3^- ion in peak-hopping mode using the SEM detector. The total procedural Os blank was 0.4 ± 2 pg (n = 5, 2 SD) contributing negligible amounts to the measured Os concentrations of all samples.

The remaining HSE concentrations were determined using a Thermo Element XR HR-ICP-MS unit at the Steinmann Institute at the University of Bonn, Germany or, in the case of samples 40R-1_28.0-30.0 and 40R-1_33.0-35.0, using a Thermo Scientific Element 2 HR-ICP-MS unit at the Vrije Universiteit Brussel, following the procedures outlined in (*53*). Briefly, instrumental mass fractionation was quantified by analyzing a 1-ppb HSE standard solution multiple times, at the beginning, middle, and end of the analytical session. To monitor isobaric and oxide interferences caused by Hf on Ir and Pt, a 1-ppb Hf solution was run at the beginning and end of each analytical session. Rhenium, Ir, and Pt were measured with a cyclonic borosilicate glass spray chamber at the University of Bonn. At the Vrije Universiteit Brussel, a CETAC Aridus II desolvating nebulizer system was used during the measurement of the individually collected Re-Ru, Pt-Ir, and Pd cuts. Total blanks for this study were 0.7 to 3 pg for Ir, 20 to 50 pg for Pt, and 2 to 5 pg for Re at the University of Bonn (n = 5). The single blank measured at the Vrije Universiteit Brussel falls within these ranges for Re, Ir, and Pt and was determined to be 2.5 pg for Ru and 6.2 pg for Pd. The total blanks thus contribute negligible amounts to the measured HSE concentrations of all samples. The 2 SE uncertainties for all measurements are less than 4%.

Repeated N-TIMS measurement (n = 3) of 10-pg loads of a DROsS (Durham Romil Osmium Standard) solution were performed using an electron multiplier at typical signal intensities of ~10,000 to ~100,000 counts/s on mass 192. The DROsS measurements yielded an average of 0.16088 ± 56 for $^{187}Os/^{188}Os$, 1.2167 ± 40 for $^{189}Os/^{188}Os$, and 1.9782 ± 80 for $^{190}Os/^{188}Os$ ratios. The long-term external reproducibility is ±0.4% for $^{187}Os/^{188}Os$, ±0.2% for $^{189}Os/^{188}Os$, and ± 0.3% for $^{190}Os/^{188}Os$. To quantify the precision and accuracy of the Os and HSE chemical and analytical procedures, we have performed replicate analyses of international reference material OKUM (IAG-certified komatiite). Averages and RSDs (% RSD) of element concentrations for HSE are indistinguishable from the literature values within 2 SE uncertainty, and $^{187}Os/^{188}Os$ data are in excellent agreement with literature data. The data for the seven samples measured at the University of Vienna and collaborating institutes are summarized in table S6.

ICP-MS at the University of Notre Dame

Determination of HSE abundances in 10 Expedition 364 samples was accomplished using ICP-MS after cation exchange chromatography to remove the matrix (table S7). Calibration was accomplished using the method of standard additions as described in (*54*). Approximately 0.1 g of powdered sample is first treated with concentrated HF and HNO_3 (3 and 4 ml, respectively) for 24 hours at 110°C. Once dried down, the sample is digested using aqua regia (HCl:HNO_3 at 3:1 ratio) in Parr Bomb pressure vessels at 150°C for another 24 hours. Once cooled to room temperature, the sample is transferred to a 15-ml Astimex Teflon digestion beaker with several rinses of 18 megohm·cm water and dried down at a temperature of 150°C. Concentrated HCl (4 ml) is added to dissolve all solids, after which the solution is evaporated to dryness. Cation exchange columns are prepared with 4 ml of Dowex AG 50 W-X8 cation exchanger, H^+ form, 200 to 400 mesh resin. The dried sample is brought up in 0.6 M HCl just before loading into a column and rinsed through using the method outlined in (*54*). The sample is then split into two equal aliquots and rinsed through two other columns, after which these are combined into a single vessel and dried down. Just before analysis, the sample is brought into solution in 3 ml of 2% HNO_3 and centrifuged to eliminate any residual resin that may have escaped the columns. The sample is then divided into three aliquots to be analyzed via standard addition. Two of the aliquots were spiked with 1 and 5 ppb of the HSEs, respectively, while the third aliquot was left unspiked. Internal standards of In and Bi (1 ppb each) were used to monitor signal drift and instrument instability. Samples were analyzed using a Nu Instruments Attom HR-ICP-MS after tuning of the instrument settings using a 1-ppb multi-element solution that yielded ~1.2 million counts/s on ^{115}In in low and ~90,000 counts/s in medium mass resolution (resolution = mass/peak width, low is ~300, medium is ~2500). All samples were analyzed at medium mass resolution.

SUPPLEMENTARY MATERIALS

Supplementary material for this article is available at http://advances.sciencemag.org/cgi/content/full/7/9/eabe3647/DC1

REFERENCES AND NOTES

1. L. W. Alvarez, W. Alvarez, F. Asaro, H. V. Michel, Extraterrestrial cause for the Cretaceous-Tertiary extinction. *Science* **208**, 1095–1108 (1980).
2. J. Smit, J. Hertogen, An extraterrestrial event at the Cretaceous–Tertiary boundary. *Nature* **285**, 198–200 (1980).
3. P. Schulte, L. Alegret, I. Arenillas, J. A. Arz, P. J. Barton, P. R. Bown, T. J. Bralower, G. L. Christeson, P. Claeys, C. S. Cockell, G. S. Collins, A. Deutsch, T. J. Goldin, K. Goto, J. M. Grajales-Nishimura, R. A. F. Grieve, S. P. S. Gulick, K. R. Johnson, W. Kiessling, C. Koeberl, D. A. Kring, K. G. MacLeod, T. Matsui, J. Melosh, A. Montanari, J. V. Morgan, C. R. Neal, D. J. Nichols, R. D. Norris, E. Pierazzo, G. Ravizza, M. Rebolledo-Vieyra, W. U. Reimold, E. Robin, T. Salge, R. P. Speijer, A. R. Sweet, J. Urrutia-Fucugauchi, V. Vajda, M. T. Whalen, P. S. Willumsen, The Chicxulub asteroid impact and mass extinction at the Cretaceous-Paleogene boundary. *Science* **327**, 1214–1218 (2010).
4. C. J. Sprain, P. R. Renne, W. A. Clemens, G. P. Wilson, Calibration of chron C29r: New high-precision geochronologic and paleomagnetic constraints from the Hell Creek region, Montana. *Geol. Soc. Am. Bull.* **130**, 1615–1644 (2018).
5. J. Smit, The global stratigraphy of the Cretaceous-Tertiary boundary impact ejecta. *Annu. Rev. Earth Planet. Sci.* **27**, 75–113 (1999).
6. P. Claeys, W. Kiessling, W. Alvarez, Distribution of Chicxulub ejecta at the Cretaceous-Tertiary boundary. *Spec. Pap. Geol. Soc. Am.* **356**, 55 (2002).
7. S. Goderis, R. Tagle, J. Belza, J. Smit, A. Montanari, F. Vanhaecke, J. Erzinger, P. Claeys, Reevaluation of siderophile element abundances and ratios across the Cretaceous–Paleogene (K–Pg) boundary: Implications for the nature of the projectile. *Geochim. Cosmochim. Acta* **120**, 417–446 (2013).
8. K. Chen, R. J. Walker, R. L. Rudnick, S. Gao, R. M. Gaschnig, I. S. Puchtel, M. Tang, Z.-C. Hu, Platinum-group element abundances and Re-Os isotopic systematics of the upper continental crust through time: Evidence from glacial diamictites. *Geochim. Cosmochim. Acta* **191**, 1–16 (2016).
9. F. M. Gradstein, J. G. Ogg, M. Schmitz, G. Ogg, *The Geologic Time Scale 2012* (Elsevier, 2012).
10. G. S. Collins, N. Patel, T. M. Davison, A. S. P. Rae, J. V. Morgan, S. P. S. Gulick; IODP-ICDP Expedition 364 Science Party and Third-Party Scientists, A steeply-inclined trajectory for the Chicxulub impact. *Nat. Commun.* **11**, 1480 (2020).
11. J. Belza, S. Goderis, A. Montanari, F. Vanhaecke, P. Claeys, Petrography and geochemistry of distal spherules from the K–Pg boundary in the Umbria–Marche region (Italy) and their origin as fractional condensates and melts in the Chicxulub impact plume. *Geochim. Cosmochim. Acta* **202**, 231–263 (2017).
12. N. Artemieva, J. Morgan, Global K-Pg layer deposited from a dust cloud. *Geophys. Res. Lett.* **47**, e2019GL086562 (2020).
13. F. T. Kyte, A meteorite from the Cretaceous/Tertiary boundary. *Nature* **396**, 237–239 (1998).
14. G. Quitté, E. Robin, S. Levasseur, F. Capmas, R. Rocchia, J.-L. Birck, C. J. Allègre, Osmium, tungsten, and chromium isotopes in sediments and in Ni-rich spinel at the K-T boundary: Signature of a chondritic impactor. *Meteorit. Planet. Sci.* **42**, 1567–1580 (2007).
15. J. Smit, A. J. T. Romein, A sequence of events across the Cretaceous-Tertiary boundary. *Earth Planet. Sci. Lett.* **74**, 155–170 (1985).
16. J. C. Sanford, J. W. Snedden, S. P. S. Gulick, The Cretaceous-Paleogene boundary deposit in the Gulf of Mexico: Large-scale oceanic basin response to the Chicxulub impact. *J. Geophys. Res. Solid Earth* **121**, 1240–1261 (2016).
17. A. R. Hildebrand, W. V. Boynton, Proximal Cretaceous-Tertiary boundary impact deposits in the Caribbean. *Science* **248**, 843–847 (1990).
18. A. R. Hildebrand, G. T. Penfield, D. A. Kring, M. Pilkingston, Z. A. Camargo, S. B. Jacobsen, W. V. Boynton, Chicxulub crater: A possible Cretaceous/Tertiary boundary impact crater on the Yucatán Peninsula, Mexico. *Geology* **19**, 867–871 (1991).
19. S. P. S. Gulick, P. J. Barton, G. L. Christeson, J. V. Morgan, M. McDonald, K. Mendoza-Cervantes, Z. F. Pearson, A. Surendra, J. Urrutia-Fucugauchi, P. M. Vermeesch, M. R. Warner, Importance of pre-impact crustal structure for the asymmetry of the Chicxulub impact crater. *Nat. Geosci.* **1**, 131–135 (2008).
20. D. A. Kring, The Chicxulub impact event and its environmental consequences at the Cretaceous-Tertiary boundary. *Palaeogeogr. Palaeocl.* **255**, 4–21 (2007).
21. P. M. Hull, A. Bornemann, D. E. Penman, M. J. Henehan, R. D. Norris, P. A. Wilson, P. Blum, L. Alegret, S. J. Batenburg, P. R. Bown, T. J. Bralower, C. Cournede, A. Deutsch, B. Donner, O. Friedrich, S. Jehle, H. Kim, D. Kroon, P. C. Lippert, D. Loroch, I. Moebius, K. Moriya, D. J. Peppe, G. E. Ravizza, U. Röhl, J. D. Schueth, J. Sepúlveda, P. F. Sexton, E. C. Sibert, K. K. Śliwińska, R. E. Summons, E. Thomas, T. Westerhold, J. H. Whiteside, T. Yamaguchi, J. C. Zachos, On impact and volcanism across the Cretaceous-Paleogene boundary. *Science* **367**, 266–272 (2020).
22. J. V. Morgan, S. P. S. Gulick, T. Bralower, E. Chenot, G. Christeson, P. Claeys, C. Cockell, G. S. Collins, M. J. L. Coolen, L. Ferrière, C. Gebhardt, K. Goto, H. Jones, D. A. Kring, E. Le Ber, J. Lofi, X. Long, C. Lowery, C. Mellett, R. Ocampo-Torres, G. R. Osinski, L. Perez-Cruz, A. Pickersgill, M. Poelchau, A. Rae, C. Rasmussen, M. Rebolledo-Vieyra, U. Riller, H. Sato, D. R. Schmitt, J. Smit, S. Tikoo, N. Tomioka, J. Urrutia-Fucugauchi, M. Whalen, A. Wittmann, K. E. Yamaguchi, W. Zylberman, The formation of peak rings in large impact craters. *Science* **354**, 878–882 (2016).
23. J. V. Morgan, S. Gulick, C. L. Mellet, S. L. Green, the Expedition 364 Scientists, *Proceedings of the International Ocean Discovery Program, Volume 364: Drilling the K-Pg impact crater* (International Ocean Discovery Program, College Station, TX, 2017).
24. C. M. Lowery, T. J. Bralower, J. D. Owens, F. J. Rodríguez-Tovar, H. Jones, J. Smit, M. T. Whalen, P. Claeys, K. Farley, S. P. S. Gulick, J. V. Morgan, S. Green, E. Chenot, G. L. Christeson, C. S. Cockell, M. J. L. Coolen, L. Ferrière, C. Gebhardt, K. Goto, D. A. Kring, J. Lofi, R. Ocampo-Torres, L. Perez-Cruz, A. E. Pickersgill, M. H. Poelchau, A. S. P. Rae, C. Rasmussen, M. Rebolledo-Vieyra, U. Riller, H. Sato, S. M. Tikoo, N. Tomioka, J. Urrutia-Fucugauchi, J. Vellekoop, A. Wittmann, L. Xiao, K. E. Yamaguchi, W. Zylberman, Rapid recovery of life at ground zero of the end-Cretaceous mass extinction. *Nature* **558**, 288–291 (2018).
25. M. T. Whalen, S. P. S. Gulick, C. M. Lowery, T. J. Bralower, J. V. Morgan, K. Grice, B. Schaefer, J. Smit, J. Ormö, A. Wittmann, D. A. Kring, S. Lyons, S. Goderis; IODP-ICDP Expedition 364 Scientists, Winding down the Chicxulub impact: The transition between impact and normal marine sedimentation near ground zero. *Mar. Geol.* **430**, 106368 (2020).
26. U. Riller, M. Poelchau, A. S. P. Rae, F. M. Schulte, G. S. Collins, J. Melosh, R. A. F. Grieve, J. V. Morgan, S. P. S. Gulick, J. Lofi, A. Diaw, N. M. Call, D. A. Kring; IODP-ICDP Expedition 364 Science Party, Rock fluidization during peak-ring formation of large impact structures. *Nature* **562**, 511–518 (2018).
27. S. P. S. Gulick, T. J. Bralower, J. Ormö, B. Hall, K. Grice, B. Schaefer, S. Lyons, K. H. Freeman, J. V. Morgan, N. Artemieva, P. Kaskes, S. J. de Graaff, M. T. Whalen, G. S. Collins, S. M. Tikoo, C. Verhagen, G. L. Christeson, P. Claeys, M. J. L. Coolen, S. Goderis, K. Goto, R. A. F. Grieve, N. McCall, G. R. Osinski, A. S. P. Rae, U. Riller, J. Smit, V. Vajda, A. Wittmann; Expedition 364 Scientists, The first day of the Cenozoic. *Proc. Natl. Acad. Sci. U.S.A.* **116**, 19342–19351 (2019).
28. M. T. Whalen, S. P. S. Gulick, Z. F. Pearson, R. D. Norris, L. Perez-Cruz, J. Urrutia-Fucugauchi, Annealing the Chicxulub impact: Paleogene Yucatán carbonate slope development in the Chicxulub impact basin, Mexico. *SEPM* **105**, 282–304 (2013).
29. T. J. Bralower, J. Cosmidis, M. S. Fantle, C. M. Lowery, B. H. Passey, S. P. S. Gulick, J. V. Morgan, V. Vajda, M. T. Whalen, A. Wittmann, N. Artemieva, K. Farley, S. Goderis, E. Hajek, P. J. Heaney, D. A. Kring, S. L. Lyons, C. Rasmussen, E. Sibert, F. J. Rodríguez Tovar, G. Turner-Walker, J. C. Zachos, J. Carte, S. A. Chen, C. Cockell, M. Coolen, K. H. Freeman, J. Garber, M. Gonzalez, J. L. Gray, K. Grice, H. L. Jones, B. Schaefer, J. Smit, S. M. Tikoo, The habitat of the nascent Chicxulub crater. *AGU Adv.* **1**, e2020AV000208 (2020).
30. C. Koeberl, V. L. Sharpton, B. C. Schuraytz, S. B. Shirey, J. D. Blum, L. E. Marin, Evidence for a meteoritic component in impact melt rock from the Chicxulub structure. *Geochim. Cosmochim. Acta* **58**, 1679–1684 (1994).
31. R. Tagle, J. Erzinger, L. Hecht, R. T. Schmitt, D. Stoeffler, P. Claeys, Platinum group elements in impactites of the ICDP Chicxulub drill core Yaxcopoil-1: Are there traces of the projectile? *Meteorit. Planet. Sci.* **39**, 1009–1016 (2004).
32. A. Gelinas, D. A. Kring, L. Zurcher, J. Urrutia-Fucugauchi, O. Morton, R. J. Walker, Osmium isotope constraints on the proportion of bolide component in Chicxulub impact melt rocks. *Meteorit. Planet. Sci.* **39**, 1003–1008 (2004).
33. V. L. Sharpton, G. B. Dalrymple, L. E. Marín, G. Ryder, B. C. Schuraytz, J. Urrutia-Fucugauchi, New links between the Chicxulub impact structure and the Cretaceous/Tertiary boundary. *Nature* **359**, 819–821 (1992).
34. B. Schmitz, P. Andersson, J. Dahl, Iridium, sulfur isotopes and rare earth elements in the Cretaceous-Tertiary boundary clay at Stevns Klint, Denmark. *Geochim. Cosmochim. Acta* **52**, 229–236 (1988).
35. J.-P. Lorand, R. H. Hewins, L. Remusat, B. Zanda, S. Pont, H. Leroux, M. Marinova, D. Jacob, M. Humayun, A. Nemchin, M. Grange, A. Kennedy, C. Göpel, Nickeliferous pyrite tracks pervasive hydrothermal alteration in Martian regolith breccia: A study in NWA 7533. *Geochim. Cosmochim. Acta* **241**, 134–149 (2018).
36. D. A. Kring, S. M. Tikoo, M. Schmieder, U. Riller, M. Rebolledo-Vieyra, S. L. Simpson, G. R. Osinski, J. Gattacceca, A. Wittmann, C. M. Verhagen, C. S. Cockell, M. J. L. Coolen, F. J. Longstaffe, S. P. S. Gulick, J. V. Morgan, T. J. Bralower, E. Chenot, G. L. Christeson, P. Claeys, L. Ferrière, C. Gebhardt, K. Goto, S. L. Green, H. Jones, J. Lofi, C. M. Lowery, R. Ocampo-Torres, L. Perez-Cruz, A. E. Pickersgill, M. H. Poelchau, A. S. P. Rae, C. Rasmussen, H. Sato, J. Smit, N. Tomioka, J. Urrutia-Fucugauchi, M. T. Whalen, L. Xiao, K. E. Yamaguchi, Probing the hydrothermal system of the Chicxulub impact crater. *Sci. Adv.* **6**, eaaz3053 (2020).
37. F. S. Paquay, G. E. Ravizza, T. K. Dalai, B. Peucker-Ehrenbrink, Determining chondritic impactor size from the marine osmium isotope record. *Science* **320**, 214–218 (2008).
38. C., T., A. Lee, G. J. Wasserburg, F. Kyte, Platinum-group elements (PGE) and rhenium in marine sediments across the Cretaceous–Tertiary boundary: Constraints on Re-PGE transport in the marine environment. *Geochim. Cosmochim. Acta* **67**, 655–670 (2003).
39. D. C. Colodner, E. A. Boyle, J. E. Edmond, J. Thomson, Post-depositional mobility of platinum, iridium and rhenium in marine sediments. *Nature* **358**, 402–404 (1992).

40. B. Schaefer, K. Grice, M. J. L. Coolen, R. E. Summons, X. Cui, T. Bauersachs, L. Schwark, M. E. Böttcher, T. J. Bralower, S. L. Lyons, K. H. Freeman, C. S. Cockell, S. P. S. Gulick, J. V. Morgan, M. T. Whalen, C. M. Lowery, V. Vajda, Microbial life in the nascent Chicxulub crater. *Geology* **48**, 328–332 (2020).
41. G. L. Christeson, S. P. S. Gulick, J. V. Morgan, C. Gebhardt, D. A. Kring, E. Le Ber, J. Lofi, C. Nixon, M. Poelchau, A. S. P. Rae, M. Rebolledo-Vieyra, U. Riller, D. R. Schmitt, A. Wittmann, T. J. Bralower, E. Chenot, P. Claeys, C. S. Cockell, M. J. L. Coolen, L. Ferrière, S. Green, K. Goto, H. Jones, C. M. Lowery, C. Mellett, R. Ocampo-Torres, L. Perez-Cruz, A. E. Pickersgill, C. Rasmussen, H. Sato, J. Smit, S. M. Tikoo, N. Tomioka, J. Urrutia-Fucugauchi, M. T. Whalen, L. Xiao, K. E. Yamaguchi, Extraordinary rocks from the peak ring of the Chicxulub impact crater: P-wave velocity, density, and porosity measurements from IODP/ICDP Expedition 364. *Earth Planet. Sci. Lett.* **495**, 1–11 (2018).
42. S. Donaldson, A. R. Hildebrand, The global fluence of iridium at the Cretaceous–Tertiary boundary. *Meteorit. Planet. Sci.* **36**, A50 (2001).
43. R. Rocchia, E. Robin, L. Froget, J. Gayraud, Stratigraphic distribution of extraterrestrial markers at the Cretaceous-Tertiary boundary in the Gulf of Mexico area: Implications for the temporal complexity of the event. *Spec. Pap. Geol. Soc. Am.* **307**, 279–286 (1996).
44. L. R. Teal, M. T. Bulling, E. R. Parker, M. Solan, Global patterns of bioturbation intensity and mixed depth of marine soft sediments. *Aquat. Biol.* **2**, 207–218 (2008).
45. F. J. Rodríguez-Tovar, C. M. Lowery, T. J. Bralower, S. P. S. Gulick, H. L. Jones, Rapid macrobenthic diversification and stabilization after the end-Cretaceous mass extinction event. *Geology* **48**, 1048–1052 (2020).
46. C. S. Cockell, G. R. Osinski, P. Lee, The impact crater as a habitat: Effects of impact processing of target materials. *Astrobiology* **3**, 181–191 (2003).
47. D. Mader, C. Koeberl, Using instrumental neutron activation analysis for geochemical analyses of terrestrial impact structures: Current analytical procedures at the University of Vienna gamma spectrometry laboratory. *Appl. Radiat. Isotopes* **67**, 2100–2103 (2009).
48. R. Das Gupta, A. Banerjee, S. Goderis, P. Claeys, F. Vanhaecke, R. Chakrabarti, Evidence for a chondritic impactor, evaporation-condensation effects and melting of the Precambrian basement beneath the 'target' Deccan basalts at Lonar crater, India. *Geochim. Cosmochim. Acta* **215**, 51–75 (2017).
49. W. Alvarez, F. Asaro, H. V. Michel, L. W. Alvarez, Iridium anomaly approximately synchronous with terminal Eocene extinctions. *Science* **216**, 886–888 (1982).
50. S. Boschi, B. Schmitz, F. Terfelt, L. Ros, M. Elfman, P. Kristiansson, C. Sulas, S. Monechi, A. Montanari, Popigai impact ejecta layer and extraterrestrial spinels recoverd in a new Italian location – The Monte Vaccaro section (Marche Apennines, Italy). *Spec. Pap. Geol. Soc. Am.* **542**, 355–367 (2019).
51. A. Ishikawa, R. Senda, K. Suzuki, C. Dale, T. C. Meisel, Re-evaluating digestion methods for highly siderophile element and ^{187}Os isotope analysis: Evidence from geological reference materials. *Chem. Geol.* **384**, 27–47 (2014).
52. T. Schulz, A. Luguet, W. Wegner, D. van Acken, C. Koeberl, Target rocks, impact glasses, and melt rocks from the Lonar crater, India: Highly siderophile element systematics and Sr-Nd-Os isotopic signatures. *Meteorit. Planet. Sci.* **51**, 1323–1339 (2016).
53. D. Van Acken, J. E. Hoffmann, J. H. D. Schorscher, T. Schulz, A. Heuser, A. Luguet, Formation of high-Al komatiites from the Mesoarchean Quebra Osso Group, Minas Gerais, Brazil: Trace elements, HSE systematics and Os isotopic signatures. *Chem. Geol.* **422**, 108–121 (2016).
54. J. C. Ely, C. R. Neal, J. A. O'Neill Jr., J. C. Jain, Quantifying the platinum group elements (PGEs) and gold in geological samples using cation exchange pretreatment and ultrasonic nebulization inductively coupled plasma-mass spectrometry (USN-ICP-MS). *Chem. Geol.* **157**, 219–234 (1999).
55. C. R. Scotese, C. Dreher, *Global Geology* (2012); www.GlobalGeology.com.
56. J. W. Snedden, W. E. Galloway, *The Gulf of Mexico Sedimentary Basin: Depositional Evolution and Petroleum Applications* (Cambridge Univ. Press, 2019).
57. P. M. Vermeesch, J. V. Morgan, Structural uplift beneath the Chicxulub impact structure. *J. Geophys. Res. Solid Earth* **113**, B07103 (2008).
58. M. Fischer-Gödde, H. Becker, F. Wombacher, Rhodium, gold and other highly siderophile element abundances in chondritic meteorites. *Geochim. Cosmochim. Acta* **74**, 356–379 (2010).
59. R. Tagle, L. Hecht, Geochemical identification of projectiles in impact rocks. *Meteorit. Planet. Sci.* **41**, 1721–1735 (2006).
60. W. v. Engelhardt, J. Arndt, B. Fecker, H. G. Pankau, Suevite breccia from the Ries crater, Germany: Origin, cooling history and devitrification of impact glasses. *Meteoritics* **30**, 279–293 (1995).
61. L. Ferrière, C. Koeberl, W. U. Reimold, Characterization of ballen quartz and cristobalite in impact breccias: New observations and constraints on ballen formation. *Eur. J. Mineral.* **21**, 203–217 (2009).
62. D. A. Kring, D. D. Durda, Trajectories and distribution of material ejected from the Chicxulub impact crater: Implications for post-impact widlfires. *J. Geophys. Res.* **107**, 10.1029/2001JE001532, (2002).
63. P. K. Abraitis, R. A. D. Pattrick, D. J. Vaughan, Variations in the compositional, textural and electrical properties of natural pyrite: A review. *Int. J. Miner. Process.* **74**, 41–59 (2004).
64. W. F. McDonough, S.-s. Sun, The composition of the Earth. *Chem. Geol.* **120**, 223–253 (1995).
65. R. L. Rudnick, S. Gao, The Crust, Vol. 3, in *Treatise on Geochemistry*, H. D. Holland, K. K. Turekian, Eds. (Elsevier-Pergamon, 2003).
66. R. Tostevin, G. A. Shields, G. M. Tarbuck, T. Ge, M. O. Clarkson, R. A. Wood, Effective use of cerium anomalies as a redox proxy in carbonate-dominated marine settings. *Chem. Geol.* **438**, 146–162 (2016).

Acknowledgments: Expedition 364 was jointly funded by the European Consortium for Ocean Research Drilling (ECORD) and the International Continental Scientific Drilling Program, with contributions and logistical support from the Yucatán State Government and Universidad Nacional Autónoma de México (UNAM). We acknowledge B. Lippens and G. Batic for support with the preparation of polished sections; **Funding:** Financial support was provided by the Belgian Federal Science Policy Office (BELSPO) project Chicxulub and Research Foundation–Flanders (FWO) project G0A6517. S.G., P.C., S.C., and F.V. thank FWO and the Fonds de la Recherche Scientifique (FNRS) for financial support through the EOS-Excellence of Science program (ET-HoME ID 30442502). S.G., P.C., P.K., J.V., S.J.d.G., and T.D. were also supported by the VUB strategic program. B.S. acknowledges the support by the K&A Wallenberg Foundation and ERC Advanced Grant ASTROGEOBIOSPHERE 213000. J.D.O. is supported by NASA Exobiology (80NSSC18K1532) and the National High Magnetic Field Laboratory (Tallahassee, Florida), which is funded by the National Science Foundation Cooperative Agreement No. DMR1644779 and the State of Florida. F.V. acknowledges BOF-UGent for financial support. Funding also came from FWO grants 11E6619N (to P.K.), 12Z6618N (to J.V.), and 12S5718N (to S.J.M.V.M.), NSF-OCE-1737087 (to A.W.), NSF-OCE-1736826 (to D.A.K. and M.Sc.), NSF-OCE-1736951 (to T.J.B.), NSF-OCE-1737199 (to M.T.W.) and NSF-OCE-1737351 (to S.P.S.G. and C.M.L.), NSF-OCE-1737155 (to C.R.N. and D.B.), and NERC NE/P005217/1 (to J.V.M.); **Author contributions:** S.G., H.S., L.F., D.B., P.C., S.P.S.G., J.V.M., J.S., and A.W. conceived and designed the study. S.G., H.S., L.F., B.S., D.B., M.E., A.I., P.K., S.M.C., C.R.N., and T.S. prepared and carried out HSE concentration and Os isotope analyses. J.D.O., J.-G.F., and C.K. determined major and trace element concentrations. S.G., N.J.d.W., and P.K. applied μXRF. S.G., L.F. and T.J.B. performed SEM-EDS, while A.W. and M.Sc. carried out and processed EMPA analyses. S.G. and S.J.M.V.M. carried out and processed LA-ICP-MS analyses. The manuscript was mainly drafted by S.G., P.C., and P.K., with major contributions from all co-authors. This is University of Texas Institute for Geophysics Contribution #3717 and Center for Planetary Systems Habitability Contribution #0022. This is LPI Contribution No. 2586. The LPI is operated by USRA under a cooperative agreement with the Science Mission Directorate of the National Aeronautics and Space Administration. This is contribution 67 of the DFG-funded ICPMS facilities at the Steinmann-Institute, University of Bonn. **Competing interests:** The authors declare that they have no competing interests. **Data and materials availability:** All data needed to evaluate the conclusions in the paper are present in the paper and/or the Supplementary Materials. This research used samples and data provided by IODP and sample requests can be made through the Sample and Data Request system http://web.iodp.tamu.edu/sdrm/. Additional data related to this paper may be requested from the authors.

Submitted 17 August 2020
Accepted 11 January 2021
Published 24 February 2021
10.1126/sciadv.abe3647

Citation: S. Goderis, H. Sato, L. Ferrière, B. Schmitz, D. Burney, P. Kaskes, J. Vellekoop, A. Wittmann, T. Schulz, S. M. Chernonozhkin, P. Claeys, S. J. de Graaff, T. Déhais, N. J. de Winter, M. Elfman, J.-G. Feignon, A. Ishikawa, C. Koeberl, P. Kristiansson, C. R. Neal, J. D. Owens, M. Schmieder, M. Sinnesael, F. Vanhaecke, S. J. M. Van Malderen, T. J. Bralower, S. P. S. Gulick, D. A. Kring, C. M. Lowery, J. V. Morgan, J. Smit, M. T. Whalen, IODP-ICDP Expedition 364 Scientists, Globally distributed iridium layer preserved within the Chicxulub impact structure. *Sci. Adv.* **7**, eabe3647 (2021).

ScienceAdvances

Globally distributed iridium layer preserved within the Chicxulub impact structure

Steven GoderisHonami SatoLudovic FerrièreBirger SchmitzDavid BurneyPim KaskesJohan VellekoopAxel WittmannToni SchulzStepan M. ChernonozhkinPhilippe ClaeysSietze J. de GraaffThomas DéhaisNiels J. de WinterMikael ElfmanJean-Guillaume FeignonAkira IshikawaChristian KoeberlPer KristianssonClive R. NealJeremy D. OwensMartin SchmiederMatthias SinnesaelFrank VanhaeckeStijn J. M. Van MaldereTimothy J. BralowerSean P. S. GulickDavid A. KringChristopher M. LoweryJoanna V. MorganJan SmitMichael T. Whalen

Sci. Adv., 7 (9), eabe3647. • DOI: 10.1126/sciadv.abe3647

Science Advances (ISSN 2375-2548) is published by the American Association for the Advancement of Science. 1200 New York Avenue NW, Washington, DC 20005. The title *Science Advances* is a registered trademark of AAAS.